

See discussions, stats, and author profiles for this publication at:  
<https://www.researchgate.net/publication/222693999>

# Conservative multigrid methods for Cahn–Hilliard fluids

ARTICLE *in* JOURNAL OF COMPUTATIONAL PHYSICS · JANUARY 2004

Impact Factor: 2.43 · DOI: 10.1016/j.jcp.2003.07.035

---

CITATIONS

157

---

READS

14

3 AUTHORS, INCLUDING:



**Junseok Kim**

Korea University

**120** PUBLICATIONS **1,159** CITATIONS

SEE PROFILE



**John Lowengrub**

University of California, Irvine

**190** PUBLICATIONS **4,668** CITATIONS

SEE PROFILE



## Conservative multigrid methods for Cahn–Hilliard fluids

Junseok Kim <sup>a</sup>, Kyungkeun Kang <sup>b</sup>, John Lowengrub <sup>a,c,\*</sup>

<sup>a</sup> *School of Mathematics, University of Minnesota, Minneapolis, MN 55455, USA*

<sup>b</sup> *Max-Planck-Institute for Mathematics in the Sciences Inselstr. 22 - 26, Leipzig D-04103, Germany*

<sup>c</sup> *Department of Mathematics, University of California at Irvine, USA*

Received 7 September 2002; received in revised form 21 July 2003; accepted 21 July 2003

### Abstract

We develop a conservative, second-order accurate fully implicit discretization of the Navier–Stokes (NS) and Cahn–Hilliard (CH) system that has an associated discrete energy functional. This system provides a diffuse-interface description of binary fluid flows with compressible or incompressible flow components [R. Soc. Lond. Proc. Ser. A Math. Phys. Eng. Sci. 454 (1998) 2617]. In this work, we focus on the case of flows containing two immiscible, incompressible and density-matched components. The scheme, however, has a straightforward extension to multi-component systems. To efficiently solve the discrete system at the implicit time-level, we develop a nonlinear multigrid method to solve the CH equation which is then coupled to a projection method that is used to solve the NS equation. We demonstrate convergence of our scheme numerically in both the presence and absence of flow and perform simulations of phase separation via spinodal decomposition. We examine the separate effects of surface tension and external flow on the decomposition. We find surface tension driven flow alone increases coalescence rates through the retraction of interfaces. When there is an applied external shear, the evolution of the flow is nontrivial and the flow morphology repeats itself in time as multiple pinchoff and reconnection events occur. Eventually, the periodic motion ceases and the system relaxes to a global equilibrium. The equilibria we observe appears has a similar structure in all cases although the dynamics of the evolution is quite different. We view the work presented in this paper as preparatory for a detailed investigation of liquid–liquid interfaces with surface tension where the interfaces separate two immiscible fluids [On the pinchoff of liquid–liquid jets with surface tension, in preparation]. To this end, we also include a simulation of the pinchoff of a liquid thread under the Rayleigh instability at finite Reynolds number.

© 2003 Elsevier B.V. All rights reserved.

**Keywords:** Cahn–Hilliard equation; Nonlinear multigrid method; Fluid flow; Interfacial tension

\* Corresponding author. Fax: +1-612-626-2017.

E-mail addresses: [jskim@math.umn.edu](mailto:jskim@math.umn.edu) (J. Kim), [kkang@mis.mpg.de](mailto:kkang@mis.mpg.de) (K. Kang), [lowengrub@math.umn.edu](mailto:lowengrub@math.umn.edu) (J. Lowengrub).

URLs: <http://www.ima.umn.edu/~junkim>, <http://www.math.umn.edu/~lowengrub>.

## 1. Introduction

The Cahn–Hilliard (CH) equation is the prototypical continuum model of phase separation. It was originally proposed by Cahn and Hilliard [35] to model binary alloys and has subsequently been adopted to model many other physical situations such as phase transitions and interface dynamics in multiphase fluids. The CH equation, even without flow, is challenging to solve numerically for two reasons. First, the equation is fourth order in space which makes straightforward difference stencils very large and introduces a severe time step restriction for stability (stiffness), i.e.,  $\Delta t \sim \Delta x^4$  for explicit methods. Second, there is nonlinearity at the lower order spatial derivatives which can also contribute to numerical stiffness.

In the absence of flow, there has been much algorithm development and many simulations of the CH equation using finite element methods (e.g. [29–34,38,40–42,44]), finite difference algorithms (e.g. [43,45,46,50]) and spectral methods (e.g. [37,48]). Most of these finite difference and finite element references use conservative algorithms with discrete energy functionals. The discretization that is closest to the one we use in this paper is given in [38] in the context of finite element methods. In [38], the CH is treated as a system where the fourth-order equation is split into two coupled second-order equations. A Crank–Nicholson type time discretization is used such that the scheme has a discrete energy functional for any value of the time step (the scheme is nonlinear at the implicit time-level). It is highly desirable to have a discrete energy functional because this can be used to prove that the numerical solution is uniformly bounded with respect to the time and space step sizes from which it follows that the scheme is stable (e.g., see [3,38]).

In the presence of flow, there has been much recent work on simulating multicomponent fluid flows using Cahn–Hilliard (diffuse interface) models. We again refer the reader the review [1] and to the discussion below for references. Recent applications of Cahn–Hilliard fluid modeling include simulations of the two- and three-dimensional Rayleigh–Taylor instability (e.g. [5,7,8]), the pinchoff of liquid–liquid jets (e.g. [6,9]), thermocapillary flow (e.g. [10,11]), mixing (e.g. [12]), contact angles and wetting phenomena (e.g. [13,14]), gravity and capillary waves (e.g. [15–17]), coalescence (e.g. [18]), reactive flows (e.g. [19]), nucleation and spinodal decomposition (e.g. [6,10,18,20–22,36]). In particular, in [10,22], the spinodal decomposition occurs in the presence of imposed temperature gradients.

In spite of these recent algorithmic developments, the numerical solution to the CH equation has remained problematic mainly due to the difficulty in solving the nonlinear CH equation at the implicit time-level and to the resolution of the extra reactive fluid stresses generated by concentration gradients that mimic surface tension. In this paper, we develop a new conservative, second-order accurate fully implicit finite difference discretization of the Navier–Stokes (NS) and CH system that has an associated discrete energy functional for any value of the time and space steps. As in [38,39], we treat the CH equation as a system of second-order equations however we use a different discrete approximation that yields enhanced stability over the method presented in [38]. This alternative approximation also allows us to extend systematically the discrete system to the case of ternary mixtures [3]; the scheme presented in [38,39] does not have such a straightforward ternary extension. A convergence proof of our algorithm is also given in [3].

To efficiently solve the discrete system at the implicit time-level, we develop a nonlinear multigrid method to solve the CH equation which is then coupled to a projection method that is used to solve the NS equation. To our knowledge this is the first work in which a nonlinear multigrid method is used to solve the CH equation and is one of the main achievements in this paper. We find that convergence of the multigrid method can be achieved with time steps that depend very weakly on the spatial grid size. In particular, convergence is obtained if  $\Delta t \approx \Delta x$  although it may be proven [3] that  $\Delta t \leq \Delta t_0$  where  $\Delta t_0$  depends only on physical parameters and is independent of  $\Delta x$ .

By using the nonlinear multigrid method to obtain the numerical solution at the implicit time-level, we gain improved numerical stability and efficiency over standard solution techniques based on Newton's method and over algorithms for which the nonlinear terms are treated as forcing functions. Our discretization also has the advantageous side-effect of improving the accuracy of the extra reactive fluid stresses.

We demonstrate convergence of our scheme numerically in both the presence and absence of flow and perform simulations of phase separation via spinodal decomposition focusing on the effects of surface tension and external flow. We find surface tension driven flow alone increases coalescence rates through the retraction of interfaces. When there is an applied external shear, the evolution of the flow is nontrivial and the flow morphology repeats itself in time as multiple pinchoff and reconnection events occur. Eventually, the periodic motion ceases and the system relaxes to a global equilibrium. The equilibria we observe appears has a similar structure in all cases although the dynamics of the evolution is quite different.

We view the work presented in this paper as preparatory for a detailed investigation of liquid–liquid interfaces with surface tension where the interfaces separate two immiscible fluids [23]. To this end, we also include a simulation of the pinchoff of a liquid thread under the Rayleigh instability at finite Reynolds number.

The contents of this paper are as follows. In Section 2, we present the coupled NS and CH equations. In Section 3, we derive the discrete scheme, demonstrate the existence of a discrete energy functional. In Section 4, we present the nonlinear multigrid method for the fully discrete system in the absence of flow. In Section 5, we present the approximate projection method used to solve the discrete generalized NS equations. In Section 6, we perform a local mode analysis for the nonlinear multigrid scheme to analyze the smoothing factor. In Section 7, we present numerical results. In Section 8, we discuss future directions and present a simulation of the break-up of a liquid thread under the Rayleigh instability. In Appendix A, the derivation of the smoothing operator for the nonlinear multigrid scheme is presented. In Appendix B, the classical Crank–Nicolson discretization of the CH equation is presented and discussed.

## 2. Governing equations

Assuming that the fluid components are incompressible with equal densities (set to one for simplicity) and that the evolution is isothermal, the non-dimensional CH model is as follows. Let  $c$  be the phase variable (i.e., concentration), then

$$c_t(\mathbf{x}, t) + \nabla \cdot (\mathbf{u}c) = \frac{1}{Pe} \nabla \cdot (M(c) \nabla \mu(\mathbf{x}, t)) \quad \text{for } (\mathbf{x}, t) \in \Omega \times [0, T] \subset \mathbb{R}^n \times \mathbb{R} \quad (1)$$

and

$$\mu(\mathbf{x}, t) = \phi(c(\mathbf{x}, t)) - \epsilon^2 \Delta c(\mathbf{x}, t), \quad (2)$$

where  $\mathbf{u}$  is the mass-averaged fluid velocity (i.e.,  $\mathbf{u} = \mathbf{u}_1 + \mathbf{u}_2$ , where  $\mathbf{u}_1$  and  $\mathbf{u}_2$  are the velocities of the two components),  $Pe$  is the diffusional Peclet number and measures the relative strengths of advection and diffusion,  $M$  is the non-dimensional mobility,  $\mu$  is the generalized chemical potential,  $\phi(c) = F'(c)$ , and  $F(c)$  is the Helmholtz free energy which is non-convex if  $T < T_c$ , to reflect the coexistence of separate phases and  $\epsilon > 0$  is a non-dimensional measure of non-locality due to the gradient energy (Cahn number) and introduces an internal length scale (interface thickness). See also [1,2,24] for further details and references. The non-dimensionalization can be found in [2,47]. Here, for simplicity, we consider a constant mobility<sup>1</sup> ( $M \equiv 1$ ) and we take  $Pe = 1$  and we use the quartic free energy  $F(c)$ , which is defined by

$$F(c) = \frac{1}{4} c^2 (c - 1)^2. \quad (3)$$

<sup>1</sup> The extension to more general  $M = M(c)$  is straightforward and will be considered in a future work [23]. See also Fig. 11 in Section 8.

Thus, the coexisting phases correspond to  $c = 0$  and 1. The natural boundary and initial conditions for the CH equation are

$$\frac{\partial c}{\partial n} = \frac{\partial \mu}{\partial n} = 0 \quad \text{and} \quad \mathbf{u} = \mathbf{0} \quad \text{on } \partial\Omega, \quad c(\mathbf{x}, 0) = c_0(\mathbf{x}), \quad \mathbf{u}(\mathbf{x}, 0) = \mathbf{0}, \quad (4)$$

where  $n$  is the normal unit vector pointing out of  $\Omega$ .

Two important features of the CH problem in the case of zero Neumann boundary conditions are the conservation of mass  $\frac{1}{|\Omega|} \int_{\Omega} c(x, t) \, d\mathbf{x}$ , and the existence of a Lyapunov(Energy) functional  $J(c)$

$$J(c) = \int_{\Omega} \left[ F(c) + \frac{\epsilon^2}{2} |\nabla c|^2 \right] d\mathbf{x} \quad (5)$$

such that

$$\frac{d}{dt} J(c) = - \int_{\Omega} |\nabla \mu|^2 d\mathbf{x},$$

in the absence of flow. The second feature plays a crucial role in the analysis of the CH equation, including the proof of the existence of a solution to the initial boundary value problem [38], and asymptotic long time behavior [51,54]. The energy functional also readily yields a pointwise estimate of  $c$  in the one-dimensional case.

In the presence of flow, the functional  $J(c)$  now may either increase or decrease in time and satisfies

$$\frac{d}{dt} J(c) + \int_{\Omega} \mu \nabla \cdot (c\mathbf{u}) \, d\mathbf{x} = - \int_{\Omega} |\nabla \mu|^2 d\mathbf{x}.$$

If the interfaces are passive, by which we mean that the concentration field  $c$  does not affect the flow field, then  $\mathbf{u}$  satisfies the classical Navier–Stokes equations and may be imposed independently of the concentration field  $c$ . If the interfaces are active, on the other hand, the velocity field  $\mathbf{u}$  depends on  $c$  through the introduction of extra stresses that mimic the surface tension between the two fluid components. In this case, the system energy is given by

$$E_{\text{tot}} = \int_{\Omega} |\mathbf{u}|^2 / 2 \, d\mathbf{x} + \frac{We_s^{-1}}{\epsilon} J(c), \quad (6)$$

where the first term is the kinetic energy of the fluid system, the second when scaled this way (note the dependence of the second term upon  $\epsilon$ ) is a measure of the surface energy and  $We_s$  is proportional to the Weber number<sup>2</sup> which measures the relative strengths of the kinetic and surface energies [2]. The velocity satisfies a generalized Navier–Stokes (NS) system:

$$\mathbf{u}_t + \mathbf{u} \cdot \nabla \mathbf{u} = -\nabla p - \frac{We_s^{-1}}{\epsilon} c \nabla \mu + \frac{1}{Re} \nabla \cdot (\eta(c) (\nabla \mathbf{u} + \nabla \mathbf{u}^T)), \quad \nabla \cdot \mathbf{u} = 0, \quad (7)$$

where the extra stress due to the concentration gradients (i.e., interfaces) is  $-\frac{We_s^{-1}}{\epsilon} c \nabla \mu$ ,  $Re$  is the Reynolds number and  $\eta$  is the non-dimensional viscosity which is assumed to depend on the mass concentration  $c$ . In [2], it is shown using the method of matched asymptotic expansions that this term converges to the classical surface tension force as  $\epsilon \rightarrow 0$ . This result has been recently made rigorous by C. Liu and S. Shkoller (preprint) where it is shown that solutions to the NS and CH equations converge to weak solutions of classical sharp interface models of interfacial flows with surface tension. This NSCH system is known as

<sup>2</sup> The exact relation is  $We = We_s / \int_0^1 \sqrt{2F(c)} \, dc$ , where  $We$  is the physical Weber number [2].

Model H in the notation of Hohenberg and Halperin [24]. We refer the reader to the recent review paper by Anderson et al. [1] and Lowengrub and Truskinovsky [2], for example, for further details on the model. The extension of this system to the more realistic case of multiphase fluids whose components have different densities is extensively discussed in [2]. The system energy, assuming no-slip ( $\mathbf{u} = 0$ ) boundary conditions, satisfies

$$\frac{d}{dt} E_{\text{tot}} = -\frac{We_s^{-1}}{\epsilon} \int_{\Omega} |\nabla \mu|^2 \, d\mathbf{x} - \frac{Re^{-1}}{2} \int_{\Omega} \eta(c) \mathbf{D} : \mathbf{D} \, d\mathbf{x}, \quad (8)$$

where  $\mathbf{D} = \nabla \mathbf{u} + \nabla \mathbf{u}^T$  is the scaled deformation tensor.

### 3. Numerical methods

In this section, we present semi-discrete and fully discrete schemes for the NSCH system. In addition, we prove discrete versions of mass conservation and energy dissipation, which immediately imply the stability of the numerical scheme (assuming that the implicit nonlinear equations can be solved).

#### 3.1. Discretization

We shall first discretize the CH equation (1) and (2) in space. Let  $[a, b]$  and  $[c, d]$  be partitioned by

$$a = x_{\frac{1}{2}} < x_{1+\frac{1}{2}} < \cdots < x_{N_x-1+\frac{1}{2}} < x_{N_x+\frac{1}{2}} = b,$$

$$c = y_{\frac{1}{2}} < y_{1+\frac{1}{2}} < \cdots < y_{N_y-1+\frac{1}{2}} < y_{N_y+\frac{1}{2}} = d$$

so that the cells  $I_{ij} = [x_{i-\frac{1}{2}}, x_{i+\frac{1}{2}}] \times [y_{j-\frac{1}{2}}, y_{j+\frac{1}{2}}]$ ,  $1 \leq i \leq N_x$ ,  $1 \leq j \leq N_y$  cover  $\Omega = [a, b] \times [c, d]$ . Let

$$\Delta x_i = x_{i+\frac{1}{2}} - x_{i-\frac{1}{2}}, \quad \Delta y_j = y_{j+\frac{1}{2}} - y_{j-\frac{1}{2}}.$$

For simplicity, we assume that the above partitions are uniform in both directions so that

$$\Delta x_i = \Delta y_j = h \quad \text{for } 1 \leq i \leq N_x, \quad 1 \leq j \leq N_y,$$

where  $h = (b - a)/N_x = (d - c)/N_y$ . Therefore

$$x_{i+\frac{1}{2}} = a + ih, \quad y_{j+\frac{1}{2}} = c + jh$$

and let  $\Omega_h = \{(x_i, y_j) : 1 \leq i \leq N_x, 1 \leq j \leq N_y\}$ , be the set of cell-centers where

$$x_i = \frac{1}{2}(x_{i-\frac{1}{2}} + x_{i+\frac{1}{2}}), \quad y_j = \frac{1}{2}(y_{j-\frac{1}{2}} + y_{j+\frac{1}{2}}).$$

The set of cell-corners is  $\Omega_{h,\frac{1}{2}} = \{(x_{i+\frac{1}{2}}, y_{j+\frac{1}{2}}) : 0 \leq i \leq N_x, 0 \leq j \leq N_y\}$ .

Since the concentration  $c$  and the chemical potential  $\mu$  satisfy Neumann boundary conditions, it is natural to define them at cell centers. Let  $c_{ij}$  and  $\mu_{ij}$  be approximations of  $c(x_i, y_j)$  and  $\mu(x_i, y_j)$ . We first implement the zero Neumann boundary condition (4) by requiring that

$$D_x c_{-\frac{1}{2},j} = D_x c_{N_x+\frac{1}{2},j} = D_y c_{i,-\frac{1}{2}} = D_y c_{i,N_y+\frac{1}{2}} = 0, \quad (9)$$

where the discrete differentiation operators are

$$D_x c_{i+\frac{1}{2},j} = \frac{1}{h}(c_{i+1,j} - c_{i,j}), \quad D_y c_{i,j+\frac{1}{2}} = \frac{1}{h}(c_{i,j+1} - c_{i,j}).$$

We then define the discrete Laplacian by

$$\Delta_d c_{ij} = \frac{1}{h} (D_x c_{i+\frac{1}{2},j} - D_x c_{i-\frac{1}{2},j}) + \frac{1}{h} (D_y c_{i,j+\frac{1}{2}} - D_y c_{i,j-\frac{1}{2}})$$

and the discrete  $L^2$  inner product by

$$(c_1, c_2)_h = h^2 \sum_{i=1}^{N_x} \sum_{j=1}^{N_y} c_{1,ij} c_{2,ij}. \quad (10)$$

For a grid function  $c$  defined at cell centers,  $D_x c$  and  $D_y c$  are defined at cell-edges, and we use the following notation:

$$\nabla_d^c c_{ij} = (D_x c_{i+\frac{1}{2},j}, D_y c_{i,j+\frac{1}{2}}),$$

to represent the discrete gradient of  $c$  at cell-edges. Correspondingly, the (MAC) divergence at cell-centers, using values from cell-edges, is

$$\tilde{\nabla}_d^c \cdot \mathbf{g}_{ij} = \frac{1}{h} (g_{i+\frac{1}{2},j}^1 - g_{i-\frac{1}{2},j}^1) + \frac{1}{h} (g_{i,j+\frac{1}{2}}^2 - g_{i,j-\frac{1}{2}}^2)$$

for a grid function  $\mathbf{g} = (g^1, g^2)$  defined on cell-edges. We can define an inner product for  $\nabla_d^c c$  on the staggered grid by

$$(\nabla_d^c c_1, \nabla_d^c c_2)_e = h^2 \left( \sum_{i=0}^{N_x} \sum_{j=1}^{N_y} D_x c_{1,i+\frac{1}{2},j} D_x c_{2,i+\frac{1}{2},j} + \sum_{i=1}^{N_x} \sum_{j=0}^{N_y} D_y c_{1,i,j+\frac{1}{2}} D_y c_{2,i,j+\frac{1}{2}} \right). \quad (11)$$

We also define discrete norms associated with (10) and (11) as

$$\|c\|^2 = (c, c)_h, \quad |c|_{e,1}^2 = (\nabla_d^c c, \nabla_d^c c)_e.$$

The time-continuous, space-discrete system that corresponds to (1)–(4) in the absence of flow is

$$\frac{d}{dt} c_{ij} = \Delta_d \mu_{ij}, \quad \mu_{ij} = \phi(c_{ij}) - \epsilon^2 \Delta_d c_{ij}, \quad (12)$$

where  $\phi$  is defined in (3) and boundary conditions are implemented using (9). It is easy to see that this discretization is second-order accurate in space and that mass is conserved identically. The scheme also has an energy functional given by the discretization of (5). We discretize (12) in time by the Crank–Nicholson type algorithm:

$$\frac{c_{ij}^{n+1} - c_{ij}^n}{\Delta t} = \Delta_d \mu_{ij}^{n+\frac{1}{2}}, \quad (13)$$

$$\mu_{ij}^{n+\frac{1}{2}} = \hat{\phi}(c_{ij}^n, c_{ij}^{n+1}) - \frac{\epsilon^2}{2} \Delta_d (c_{ij}^n + c_{ij}^{n+1}), \quad (14)$$

where

$$\hat{\phi}(c_1, c_2) = \phi(c_2) - \frac{1}{2} \phi'(c_2)(c_2 - c_1) + \frac{1}{3!} \phi''(c_2)(c_2 - c_1)^2. \quad (15)$$

This is obtained by using the Taylor expansion of  $(F(c_1) - F(c_2))/(c_1 - c_2)$  and retaining terms up to the second-order derivative. This is a modification of the scheme presented in [38], where  $\hat{\phi}(c_1, c_2)$  was taken to be:

$$\hat{\phi}(c_1, c_2) = \begin{cases} \frac{F(c_1) - F(c_2)}{c_1 - c_2} & \text{if } c_1 \neq c_2, \\ \phi(c_1) & \text{if } c_1 = c_2. \end{cases}$$

And unlike the scheme in [38], our modified scheme can be easily extended to multi-component systems.

In the presence of flow  $\mathbf{u} = (u, v) \neq 0$ , we use the center difference operator to define the discrete gradient and divergence operators at cell-centers, respectively, by

$$\begin{aligned} \nabla_d c_{ij} &= \frac{1}{2} \left( D_x c_{i+\frac{1}{2},j} + D_x c_{i-\frac{1}{2},j}, D_y c_{i,j+\frac{1}{2}} + D_y c_{i,j-\frac{1}{2}} \right), \\ \nabla_d \cdot \mathbf{u}_{ij} &= \frac{1}{2} \left( D_x u_{i+\frac{1}{2},j} + D_x u_{i-\frac{1}{2},j} \right) + \frac{1}{2} \left( D_y v_{i,j+\frac{1}{2}} + D_y v_{i,j-\frac{1}{2}} \right). \end{aligned}$$

The non-slip boundary conditions are implemented by introducing a ring of ghost-cells surrounding the physical domain such that sum of the velocities (at cell-centers) are equal to zero on the physical boundary, i.e.,

$$\mathbf{u}_{0,j} = -\mathbf{u}_{1,j}, \quad \mathbf{u}_{N_x+1,j} = -\mathbf{u}_{N_x,j}, \quad \mathbf{u}_{i,0} = -\mathbf{u}_{i,1} \quad \text{and} \quad \mathbf{u}_{i,N_y+1} = -\mathbf{u}_{i,N_y}. \quad (16)$$

Accordingly, Eq. (13) becomes by

$$\frac{c_{ij}^{n+1} - c_{ij}^n}{\Delta t} + \nabla_d \cdot \left( \mathbf{u}_{ij}^{n+\frac{1}{2}} c_{ij}^{n+\frac{1}{2}} \right) = \Delta_d \mu_{ij}^{n+\frac{1}{2}}, \quad (17)$$

where  $\mathbf{u}^{n+\frac{1}{2}} = (\mathbf{u}^{n+1} + \mathbf{u}^n)/2$ , and  $c^{n+\frac{1}{2}}$  is defined analogously. The chemical potential  $\mu_{ij}^{n+\frac{1}{2}}$  is still obtained from (14).

For active interfaces, the velocity  $\mathbf{u}$  satisfies the generalized Navier–Stokes equations (7). Here, we will use the rotation form (i.e.,  $\mathbf{u} \cdot \nabla \mathbf{u} = \omega \times \mathbf{u} + \frac{1}{2} \nabla |\mathbf{u}|^2$ ) of the equations, together with the Bernoulli pressure  $P = p + \frac{1}{2} |\mathbf{u}|^2$ . To solve this system, we will use a projection method. Following [27], the velocity components are defined at cell-centers, where  $\mathbf{u}_{ij} \approx \mathbf{u}(x_i, y_j)$  and the pressure is defined at cell-corners ( $\Omega_{h,\frac{1}{2}}$ ), where  $P_{i+\frac{1}{2},j+\frac{1}{2}} \approx P(x_{i+\frac{1}{2}}, y_{j+\frac{1}{2}})$ . In the corresponding discrete system, we additionally define gradient and divergence operators taking values from cell-centers to cell-corners and vice versa. These operators are:

$$\begin{aligned} \nabla_d^c \cdot \mathbf{u}_{i+\frac{1}{2},j+\frac{1}{2}} &= \frac{1}{2} \left( D_x u_{i+\frac{1}{2},j} + D_x u_{i+\frac{1}{2},j-1} \right) + \frac{1}{2} \left( D_y v_{i,j+\frac{1}{2}} + D_y v_{i-1,j+\frac{1}{2}} \right), \\ \tilde{\nabla}_d^c P_{i,j} &= \frac{1}{2h} \left( P_{i+\frac{1}{2},j+\frac{1}{2}} + P_{i+\frac{1}{2},j-\frac{1}{2}} - P_{i-\frac{1}{2},j+\frac{1}{2}} - P_{i-\frac{1}{2},j-\frac{1}{2}}, P_{i+\frac{1}{2},j+\frac{1}{2}} - P_{i+\frac{1}{2},j-\frac{1}{2}} + P_{i-\frac{1}{2},j+\frac{1}{2}} - P_{i-\frac{1}{2},j-\frac{1}{2}} \right). \end{aligned}$$

We also introduce two Laplace operators that operate on cell-corners:

$$\Delta_d^c \psi_{i+\frac{1}{2},j+\frac{1}{2}} = \frac{\psi_{i-\frac{1}{2},j+\frac{1}{2}} + \psi_{i+\frac{1}{2},j+\frac{3}{2}} - 4\psi_{i+\frac{1}{2},j+\frac{1}{2}} + \psi_{i+\frac{1}{2},j-\frac{1}{2}} + \psi_{i+\frac{3}{2},j+\frac{1}{2}}}{h^2},$$

and

$$\nabla_d^c \cdot \tilde{\nabla}_d^c \psi_{i+\frac{1}{2},j+\frac{1}{2}} = \frac{\psi_{i-\frac{1}{2},j-\frac{1}{2}} + \psi_{i+\frac{3}{2},j+\frac{1}{2}} - 4\psi_{i+\frac{1}{2},j+\frac{1}{2}} + \psi_{i-\frac{1}{2},j-\frac{3}{2}} + \psi_{i+\frac{3}{2},j+\frac{3}{2}}}{2h^2}.$$

To discretize the flow equations, we then use an approximate projection method (e.g., see [27,28]). In this scheme, the incompressibility condition can be posed as

$$\nabla_d^c \cdot \left( \frac{\mathbf{u}^{n+1} - \mathbf{u}^n}{\Delta t} \right) = \Delta_t \left( \Delta_d^c - \nabla_d^c \cdot \tilde{\nabla}_d^c \right) \mathcal{L}^{-1} \left( \frac{P^{n+\frac{1}{2}} - P^{n-\frac{1}{2}}}{\Delta t} \right), \quad (18)$$



where  $\mathcal{L} = I - \frac{\Delta t}{2Re} \Delta_d^c$  and  $I$  is the identity operator. See Section 5 for a derivation. Note that the difference  $\Delta_d^c - \nabla_d^c \cdot \tilde{\nabla}_d^c$  applied to a smooth function converges to zero with second-order accuracy. If  $\Delta_d^c$  was taken to be  $\nabla_d^c \cdot \tilde{\nabla}_d^c$ , then the velocity is divergence-free on the discrete level. However, the corresponding exact projection method is ill-conditioned since the stencil for the pressure solve is algebraically decoupled (e.g., see [49]).

Finally, the discretized momentum equation is

$$\begin{aligned} \frac{\mathbf{u}_{ij}^{n+1} - \mathbf{u}_{ij}^n}{\Delta t} = & -\omega_{ij}^{n+\frac{1}{2}} \times \mathbf{u}_{ij}^{n+\frac{1}{2}} - \tilde{\nabla}_d^c P_{ij}^{n+\frac{1}{2}} + \delta \mathbf{u}_{ij}^{n+\frac{1}{2}} - \frac{We_s^{-1}}{\epsilon} c_{ij}^{n+\frac{1}{2}} \nabla_d \mu_{ij}^{n+\frac{1}{2}} + \frac{1}{Re} \nabla_d \cdot \left( \eta (c_{ij}^{n+\frac{1}{2}}) \mathbf{D}_{ij}^{n+\frac{1}{2}} \right) \\ & + \frac{\Delta t^2}{2Re} \nabla_d \cdot \left( \eta (c^{n+\frac{1}{2}}) \left( \nabla_d \tilde{\nabla}_d^c + \nabla_d^T \tilde{\nabla}_d^c - \Delta_d^c I \right) \mathcal{L}^{-1} \left( \frac{P^{n+\frac{1}{2}} - P^{n-\frac{1}{2}}}{\Delta t} \right) \right), \end{aligned} \quad (19)$$

where the vorticity is  $\omega_{ij}^{n+\frac{1}{2}} = \nabla_d \times \mathbf{u}_{ij}^{n+\frac{1}{2}}$ , and the (scaled) rate of deformation tensor is  $\mathbf{D}_{ij}^{n+\frac{1}{2}} = \nabla_d \mathbf{u}_{ij}^{n+\frac{1}{2}} + (\nabla_d \mathbf{u}_{ij}^{n+\frac{1}{2}})^T$ . The last term in Eq. (19) arises in the projection method by replacing an intermediate velocity that consists of the projected velocity at the  $n+1$  step and a pressure update. A step and a pressure update. As far as we know, this term has not been presented in other papers utilizing the projection method. Again, see Section 5 for a derivation. If the viscosity  $\eta$  is constant, the latter two viscous terms in Eq. (19) are replaced by the single term  $Re^{-1} \Delta_d \mathbf{u}^{n+\frac{1}{2}}$ . We include the more general case here for completeness although in this paper we focus on the case in which  $\eta$  constant. The case with non-constant  $\eta$  will be considered in another paper [23].

If  $\eta$  is constant and one uses the replacement described above, then  $\delta$  in Eq. (19) is given by

$$\delta = (\mathbf{u}^{n+\frac{1}{2}}, \tilde{\nabla}_d^c P^{n+\frac{1}{2}})_h / \|\mathbf{u}^{n+\frac{1}{2}}\|^2, \quad (20)$$

in order to remove the components of  $\tilde{\nabla}_d^c P_{ij}^{n+\frac{1}{2}}$  that are not orthogonal to  $\mathbf{u}_{ij}^{n+\frac{1}{2}}$  in the discrete  $L^2$  space. Note that on the continuous level,  $\delta = 0$ . Indeed, as we demonstrate in Section 7,  $\delta$  converges to zero with second-order accuracy. On the discrete level this term ensures, as we will demonstrate in the next section, that the discrete system (17)–(19) in fact has an energy functional given by the discretization of (6). For non-constant  $\eta$ , the projection factor should be taken to be [23]:

$$\delta = \left( \mathbf{u}^{n+\frac{1}{2}}, \tilde{\nabla}_d^c P^{n+\frac{1}{2}} \right)_h / \|\mathbf{u}^{n+\frac{1}{2}}\|^2 - \frac{\left( \mathbf{u}^{n+\frac{1}{2}}, \nabla_d \cdot \eta (c^{n+\frac{1}{2}}) \left( \nabla_d \tilde{\nabla}_d^c + \nabla_d^T \tilde{\nabla}_d^c - \Delta_d^c I \right) \mathcal{L}^{-1} \left( \frac{P^{n+\frac{1}{2}} - P^{n-\frac{1}{2}}}{\Delta t} \right) \right)_h}{2\Delta t^{-2} Re \|\mathbf{u}^{n+\frac{1}{2}}\|^2}. \quad (21)$$

The numerical implementation of Eqs. (13), (14) and (18)–(20) is discussed in Sections 4 and 5 where it is shown how the implicit solutions at time  $t_{n+1}$  are obtained using multigrid methods.

### 3.2. Properties of schemes

We next demonstrate a number of properties of the numerical schemes. At this stage, we assume there are no restrictions to solving the implicit systems of equations. Later, we examine the effectiveness of the multigrid algorithms used to solve the implicit equations. Before we proceed, we first state without proof the following lemma which is a easy consequence of discrete summation by parts.

**Lemma 1.** Let  $c_1$  and  $c_2$  be defined on  $\Omega_h$  satisfying (9). Let  $\mathbf{u}$  be defined on  $\Omega_h$  and satisfy (16). Finally, let  $P$  be defined on  $\Omega_{h,\frac{1}{2}}$ . Then,

$$(c_1, \Delta_d c_2)_h = (\Delta_d c_1, c_2)_h = -(\nabla_d^c c_1, \nabla_d^c c_2)_e, \quad (22)$$

$$(\mathbf{u}, \nabla_d c_1)_h = -(\nabla_d \cdot \mathbf{u}, c_1)_h, \quad (23)$$

$$(\mathbf{u}, \tilde{\nabla}_d^c P)_h = -(\nabla_d^c \cdot \mathbf{u}, P)_{h, \frac{1}{2}}, \quad (24)$$

where the cell-corner inner product is given by the trapezoidal rule approximation of the continuous inner product:

$$(\nabla_d^c \cdot \mathbf{u}, P)_{h, \frac{1}{2}} = \frac{h^2}{2} \sum_{i=0}^{N_x} \sum_{j=0}^{N_y} \nabla_d^c \cdot \mathbf{u}_{i+\frac{1}{2}, j+\frac{1}{2}} P_{i+\frac{1}{2}, j+\frac{1}{2}} + \frac{h^2}{2} \sum_{i=1}^{N_x-1} \sum_{j=1}^{N_y-1} \nabla_d^c \cdot \mathbf{u}_{i+\frac{1}{2}, j+\frac{1}{2}} P_{i+\frac{1}{2}, j+\frac{1}{2}}.$$

The following theorem establishes the mass conservation and the existence of a discrete energy functional in the absence of flow.

**Theorem 2.** If  $\{c^n, \mu^{n+\frac{1}{2}}\}$  is the solution of (13) and (14) and if we define the discrete energy functional by

$$\mathcal{F}_h(c) = (F(c), 1)_h + \frac{\epsilon^2}{2} |c|_{e,1}^2, \quad (25)$$

where  $F$  is defined in (3), then

$$(c^{n+1}, 1)_h = (c^n, 1)_h,$$

and

$$\mathcal{F}_h(c^{n+1}) - \mathcal{F}_h(c^n) = -\Delta t |\mu^{n+\frac{1}{2}}|_{e,1}^2 - \frac{1}{4} ((c^{n+1} - c^n)^4, 1)_h. \quad (26)$$

**Proof.** The first assertion is due to the combination of (13) and the discrete version of integration by parts in Lemma 1. Indeed,

$$(c^{n+1}, 1)_h = (c^n, 1)_h + \Delta t (\Delta_d \mu^{n+\frac{1}{2}}, 1)_h = (c^n, 1)_h - \Delta t (\nabla_d \mu^{n+\frac{1}{2}}, \nabla_d 1)_e = (c^n, 1)_h.$$

It remains to prove the second assertion. Multiplying  $\mu^{n+\frac{1}{2}}$  and  $c^{n+1} - c^n$  to (13) and (14), respectively, and summing by parts, we obtain the following two identities

$$(c^{n+1} - c^n, \mu^{n+\frac{1}{2}})_h + \Delta t |\mu^{n+\frac{1}{2}}|_{e,1}^2 = 0,$$

$$(c^{n+1} - c^n, \mu^{n+\frac{1}{2}})_h - \frac{\epsilon^2}{2} |c^{n+1}|_{e,1}^2 + \frac{\epsilon^2}{2} |c^n|_{e,1}^2 = (\hat{\phi}(c^n, c^{n+1}), c^{n+1} - c^n)_h.$$

Using the identities above, we obtain

$$\begin{aligned} \mathcal{F}_h(c^{n+1}) - \mathcal{F}_h(c^n) &= \frac{\epsilon^2}{2} |c^{n+1}|_{e,1}^2 - \frac{\epsilon^2}{2} |c^n|_{e,1}^2 + (F(c^{n+1}) - F(c^n), 1)_h \\ &= -\Delta t |\mu^{n+\frac{1}{2}}|_{e,1}^2 - (\hat{\phi}(c^n, c^{n+1}), c^{n+1} - c^n)_h + (F(c^{n+1}) - F(c^n), 1)_h. \end{aligned}$$

From the Taylor expansion, we have

$$\begin{aligned} F(c^{n+1}) - F(c^n) &= \phi(c^{n+1})(c^{n+1} - c^n) - \frac{1}{2} \phi'(c^{n+1})(c^{n+1} - c^n)^2 + \frac{1}{3!} \phi''(c^{n+1})(c^{n+1} - c^n)^3 \\ &\quad - \frac{1}{4!} \phi'''(c^{n+1})(c^{n+1} - c^n)^4. \end{aligned}$$

Since  $\phi'''(c^{n+1}) = 6$ , we obtain

$$\begin{aligned}\mathcal{F}_h(c^{n+1}) - \mathcal{F}_h(c^n) + \Delta t |\mu^{n+\frac{1}{2}}|_{e,1}^2 &= -(\hat{\phi}(c^n, c^{n+1}), c^{n+1} - c^n)_h + (F(c^{n+1}) - F(c^n), 1)_h \\ &= -\frac{6}{4!}((c^{n+1} - c^n)^4, 1)_h = -\frac{1}{4}((c^{n+1} - c^n)^4, 1)_h.\end{aligned}$$

This completes the proof.  $\square$

**Remark 3.** From Theorem 2, it follows that the numerical solution  $\|c^n\|$  is bounded (assuming that it is possible to solve the nonlinear scheme at the implicit time-level). This yields stability (in discrete  $L_2$ ) of the numerical scheme. It can be proven [3] that the implicit scheme has a unique solution for  $\Delta t \leq \Delta t_0(\epsilon, \phi)$ . The numerical solution of the equations at the implicit time-level is discussed in Sections 4 and 6.1, where, respectively, the nonlinear multigrid is presented and the weak time step restrictions  $\Delta t \leq \Delta t_0(\epsilon, \phi)$  or  $\Delta t \sim h$  are shown to be sufficient to obtain convergence of the nonlinear multigrid method.

**Remark 4.** The presence of the second term on the right-hand side of Eq. (26) suggests that our method is more stable than that of [38] where this term is absent.

**Remark 5.** Theorem 2 still holds for regular solution model free energies of the form [32]:

$$F(c) := \theta[c \ln(c) + (1 - c) \ln(1 - c)] - 2\theta_c c(1 - c),$$

( $\theta$  and  $\theta_c$  are the absolute and the critical temperatures, respectively) provided that they are regularized by fourth-order polynomials near the singular points, i.e.,

$$F_\delta(c) = \begin{cases} p_l(c) & \text{if } c \leq \delta, \\ F(c) & \text{if } \delta < c < 1 - \delta, \\ p_r(c) & \text{if } c \geq 1 - \delta, \end{cases}$$

where  $p_l(c)$  and  $p_r(c)$  are fourth-order polynomials which match values with  $F(c)$  up to fourth-order derivatives at  $c = \delta$  and  $c = 1 - \delta$ , respectively, and  $\delta$  is a small positive parameter.

Next, we demonstrate the existence of an energy functional in the presence of flow. For simplicity, we state and prove the theorem for the case in which the viscosity  $\eta$  is constant.

**Theorem 6.** Let  $\{c^n, \mu^{n+\frac{1}{2}}, \mathbf{u}^n\}$  be the solutions of (14) and (17), and (18) and (19) with  $\eta$  constant and let the discrete total energy functional be

$$\mathcal{E}_h(c, \mathbf{u}) = \frac{1}{2}(\mathbf{u}, \mathbf{u})_h + \frac{We_s^{-1}}{\epsilon} \left( (F(c), 1)_h + \frac{\epsilon^2}{2} |c|_1^2 \right), \quad (27)$$

then

$$\frac{\mathcal{E}_h(c^{n+1}, \mathbf{u}^{n+1}) - \mathcal{E}_h(c^n, \mathbf{u}^n)}{\Delta t} = -\frac{1}{Re} \left( |u^{n+\frac{1}{2}}|_{e,1}^2 + |v^{n+\frac{1}{2}}|_{e,1}^2 \right) - \frac{We_s^{-1}}{\epsilon} |\mu^{n+\frac{1}{2}}|_{e,1}^2 - \frac{We_s^{-1}}{4\epsilon\Delta t} ((c^{n+1} - c^n)^4, 1)_h. \quad (28)$$

**Proof.** Multiply Eq. (19) by  $\mathbf{u}^{n+\frac{1}{2}}$  and sum over cell-centers to get

$$\begin{aligned} \frac{(\mathbf{u}^{n+1}, \mathbf{u}^{n+1})_h - (\mathbf{u}^n, \mathbf{u}^n)_h}{2\Delta t} &= -(\mathbf{u}^{n+\frac{1}{2}}, \tilde{\nabla}_d^c P^{n+\frac{1}{2}})_h + \delta(\mathbf{u}^{n+\frac{1}{2}}, \mathbf{u}^{n+\frac{1}{2}})_h - \frac{We_s^{-1}}{\epsilon} (\mathbf{u}^{n+\frac{1}{2}} c^{n+\frac{1}{2}}, \nabla_d \mu^{n+\frac{1}{2}})_h \\ &\quad + \frac{1}{Re} (\mathbf{u}^{n+\frac{1}{2}}, \Delta_d \mathbf{u}^{n+\frac{1}{2}})_h \\ &= \frac{We_s^{-1}}{\epsilon} (\nabla_d \cdot (\mathbf{u}^{n+\frac{1}{2}} c^{n+\frac{1}{2}}), \mu^{n+\frac{1}{2}})_h - \frac{1}{Re} (|\mathbf{u}^{n+\frac{1}{2}}|_{e,1}^2 + |\mathbf{v}^{n+\frac{1}{2}}|_{e,1}^2), \end{aligned} \quad (29)$$

where we have used the value of  $\delta$  from Eq. (20) and we have summed by parts using Lemma 1. Next, multiply Eq. (13) by  $\mu^{n+\frac{1}{2}}$  and sum to get

$$\begin{aligned} (c^{n+1} - c^n, \mu^{n+\frac{1}{2}})_h &= -\Delta t (\nabla_d \cdot (c^{n+\frac{1}{2}} \mathbf{u}^{n+\frac{1}{2}}), \mu^{n+\frac{1}{2}})_h + \Delta t (\Delta_d \mu^{n+\frac{1}{2}}, \mu^{n+\frac{1}{2}})_h \\ &= -\Delta t (\nabla_d \cdot (c^{n+\frac{1}{2}} \mathbf{u}^{n+\frac{1}{2}}), \mu^{n+\frac{1}{2}})_h - \Delta t |\mu^{n+\frac{1}{2}}|_{e,1}^2. \end{aligned} \quad (30)$$

Combining Eqs. (29) and (30) and using the argument in the proof of Theorem 2, we obtain

$$\mathcal{E}_h(c^{n+1}, \mathbf{u}^{n+1}) - \mathcal{E}_h(c^n, \mathbf{u}^n) = -\frac{\Delta t}{Re} (|\mathbf{u}^{n+\frac{1}{2}}|_{e,1}^2 + |\mathbf{v}^{n+\frac{1}{2}}|_{e,1}^2) - \frac{We_s^{-1} \Delta t}{\epsilon} |\mu^{n+\frac{1}{2}}|_{e,1}^2 - \frac{We_s^{-1}}{4\epsilon} ((c^{n+1} - c^n)^4, 1)_h,$$

where we have used that the terms that couple flow with concentration in the equations cancel one another exactly. This completes the proof of the theorem.  $\square$

**Remark 7.** From Theorem 6, it follows that both  $\|c^n\|$  and  $\|\mathbf{u}^n\|$  are bounded uniformly in  $n$ . This yields stability (in discrete  $L_2$ ) of the numerical scheme in the presence of flow where again we have assumed that it is possible to solve the equations at the implicit time-level.

**Remark 8.** Using the more general discretization (19) and the choice of  $\delta$  given in (21), the theorem also holds if the viscosity  $\eta$  is not constant.

#### 4. Solution of the system in absence of flow

In this section, we develop a nonlinear Full Approximation Storage (FAS) multigrid method to solve the nonlinear discrete CH system (13) and (14) at the implicit time-level in the absence of flow. The fundamental idea of nonlinear multigrid is analogous to the linear case. First, the errors to the solution have to be smoothed so that they can be approximated on a coarser grid. An analogue of the linear defect equation is transformed to the coarse grid. The coarse grid corrections are interpolated back to the fine grid, where the errors are again smoothed. However, because the system is nonlinear we do not work with the errors, but rather with full approximations to the discrete solution on the coarse grid. The nonlinearity is treated using one step of Newton's iteration and a pointwise Gauss–Seidel relaxation scheme is used as the smoother in the multigrid method. This corresponds to a local rather than global linearization of the nonlinear scheme and as such is more efficient than standard Newton–Gauss–Seidel global linearization schemes. See the reference text [53] for additional details and background.

Let us rewrite equations (13), (14) as follows:

$$\text{NSO}(c^n, c^{n+1}, \mu^{n+\frac{1}{2}}) = (f^n, g^n),$$

where

$$\text{NSO}(c^n, c^{n+1}, \mu^{n+\frac{1}{2}}) = \left( \frac{c_{ij}^{n+1}}{\Delta t} - \Delta_d \mu_{ij}^{n+\frac{1}{2}}, \mu_{ij}^{n+\frac{1}{2}} - \hat{\phi}(c_{ij}^n, c_{ij}^{n+1}) + \frac{\epsilon^2}{2} \Delta_d c_{ij}^{n+1} \right),$$

and the source term is

$$(f^n, g^n) = \left( \frac{c_{ij}^n}{\Delta t}, -\frac{\epsilon^2}{2} \Delta_d c_{ij}^n \right).$$

In the following description of one FAS cycle, we assume a sequence of grids  $\Omega_k$  ( $\Omega_{k-1}$  is coarser than  $\Omega_k$  by factor 2). Given the number  $v$  of pre- and post-smoothing relaxation sweeps, an iteration step for the nonlinear multigrid method using the  $V$ -cycle is formally written as follows:

#### 4.1. FAS multigrid cycle

$$\{c_k^{m+1}, \mu_k^{m+\frac{1}{2}}\} = \text{FAScycle}(k, c_k^n, c_k^m, \mu_k^{m-\frac{1}{2}}, \text{NSO}_k, f_k^n, g_k^n, v).$$

That is,  $\{c_k^m, \mu_k^{m-\frac{1}{2}}\}$  and  $\{c_k^{m+1}, \mu_k^{m+\frac{1}{2}}\}$  are the approximations of  $c_k(x_i, y_j)$  and  $\mu_k(x_i, y_j)$  before and after a FAScycle. Now, we define the FAScycle.

##### (1) Pre-smoothing

Compute  $\{c_k^m, \bar{\mu}_k^{m-\frac{1}{2}}\}$  by applying  $v$  smoothing steps to  $\{c_k^m, \mu_k^{m-\frac{1}{2}}\}$

$$\{c_k^m, \bar{\mu}_k^{m-\frac{1}{2}}\} = \text{SMOOTH}^v(c_k^n, c_k^m, \mu_k^{m-\frac{1}{2}}, \text{NSO}_k, f_k^n, g_k^n),$$

which means performing  $v$  smoothing steps with initial approximation  $c_k^m, \mu_k^{m-\frac{1}{2}}, c_k^n$ , source terms  $f_k^n, g_k^n$ , and the SMOOTH relaxation operator (see Appendix A for its derivation) to get the approximation  $c_k^m, \bar{\mu}_k^{m-\frac{1}{2}}$ .

One SMOOTH relaxation operator step consists of solving the system (31) and (32) given below by  $2 \times 2$  matrix inversion for each  $i$  and  $j$ .

$$\frac{\bar{c}_{ij}^m}{\Delta t} + \left( \frac{2}{\Delta x^2} + \frac{2}{\Delta y^2} \right) \bar{\mu}_{ij}^{m-\frac{1}{2}} = \frac{\mu_{i+1,j}^{m-\frac{1}{2}} + \bar{\mu}_{i-1,j}^{m-\frac{1}{2}}}{\Delta x^2} + \frac{\mu_{i,j+1}^{m-\frac{1}{2}} + \bar{\mu}_{i,j-1}^{m-\frac{1}{2}}}{\Delta y^2} + f_{ij}^n \quad (31)$$

and

$$\begin{aligned} - \left[ \frac{\epsilon^2}{2} \left( \frac{2}{\Delta x^2} + \frac{2}{\Delta y^2} \right) + \frac{\partial \hat{\phi}(c_{ij}^n, c_{ij}^m)}{\partial v} \right] \bar{c}_{ij}^m + \bar{\mu}_{ij}^{m-\frac{1}{2}} &= g_{ij}^n + \hat{\phi}(c_{ij}^n, c_{ij}^m) - \frac{\partial \hat{\phi}(c_{ij}^n, c_{ij}^m)}{\partial v} c_{ij}^m - \frac{\epsilon^2}{2\Delta x^2} (c_{i+1,j}^m + \bar{c}_{i-1,j}^m) \\ &\quad - \frac{\epsilon^2}{2\Delta y^2} (c_{i,j+1}^m + \bar{c}_{i,j-1}^m). \end{aligned} \quad (32)$$

##### (2) Compute the defect

$$(\bar{d}_{1_k}^m, \bar{d}_{2_k}^m) = (f_k^n, g_k^n) - \text{NSO}_k(\bar{c}_k^m, \bar{\mu}_k^{m-\frac{1}{2}}).$$

##### (3) Restrict the defect and $\{\bar{c}_k^m, \bar{\mu}_k^{m-\frac{1}{2}}\}$

$$(\bar{d}_{1_{k-1}}^m, \bar{d}_{2_{k-1}}^m) = I_k^{k-1}(\bar{d}_{1_k}^m, \bar{d}_{2_k}^m), (\bar{c}_{k-1}^m, \bar{\mu}_{k-1}^{m-\frac{1}{2}}) = I_k^{k-1}(\bar{c}_k^m, \bar{\mu}_k^{m-\frac{1}{2}}).$$

The restriction operator  $I_k^{k-1}$  maps  $k$ -level functions to  $(k-1)$ -level functions:

$$\begin{aligned}
d_{k-1}(x_i, y_j) &= I_k^{k-1} d_k(x_i, y_j) \\
&= \frac{1}{4} \left[ d_k\left(x_i - \frac{h}{2}, y_j - \frac{h}{2}\right) + d_k\left(x_i - \frac{h}{2}, y_j + \frac{h}{2}\right) \right. \\
&\quad \left. + d_k\left(x_i + \frac{h}{2}, y_j - \frac{h}{2}\right) + d_k\left(x_i + \frac{h}{2}, y_j + \frac{h}{2}\right) \right].
\end{aligned}$$

That is, coarse grid values are obtained by averaging the four nearby fine grid values.

(4) Compute the right-hand side

$$(f_{k-1}^n, g_{k-1}^n) = (\bar{d}_{1_{k-1}}^m, \bar{d}_{2_{k-1}}^m) + \text{NSO}_{k-1}(\bar{c}_{k-1}^n, \bar{c}_{k-1}^m, \bar{\mu}_{k-1}^{m-\frac{1}{2}}).$$

(5) Compute an approximate solution  $\{\hat{c}_{k-1}^m, \hat{\mu}_{k-1}^{m-\frac{1}{2}}\}$  of the coarse grid equation on  $\Omega_{k-1}$ , i.e., solve

$$\text{NSO}_{k-1}(c_{k-1}^n, \hat{c}_{k-1}^m, \hat{\mu}_{k-1}^{m-\frac{1}{2}}) = (f_{k-1}^n, g_{k-1}^n). \quad (33)$$

If  $k = 1$ , we explicitly invert a  $2 \times 2$  matrix to obtain the solution. If  $k > 1$ , we solve (33) by performing a FAS  $k$ -grid cycle using  $\{\bar{c}_{k-1}^m, \bar{\mu}_{k-1}^{m-\frac{1}{2}}\}$  as an initial approximation:

$$\{\hat{c}_{k-1}^m, \hat{\mu}_{k-1}^{m-\frac{1}{2}}\} = \text{FAScycle}(k-1, c_{k-1}^n, \bar{c}_{k-1}^m, \bar{\mu}_{k-1}^{m-\frac{1}{2}}, \text{NSO}_{k-1}, f_{k-1}^n, g_{k-1}^n, v).$$

(6) Compute the coarse grid correction (CGC):

$$\hat{v}_{1_{k-1}}^m = \hat{c}_{k-1}^m - \bar{c}_{k-1}^m, \quad \hat{v}_{2_{k-1}}^{m-\frac{1}{2}} = \hat{\mu}_{k-1}^{m-\frac{1}{2}} - \bar{\mu}_{k-1}^{m-\frac{1}{2}}.$$

(7) Interpolate the correction

$$\hat{v}_{1_k}^m = I_{k-1}^k \hat{v}_{1_{k-1}}^m, \quad \hat{v}_{2_k}^{m-\frac{1}{2}} = I_{k-1}^k \hat{v}_{2_{k-1}}^{m-\frac{1}{2}}.$$

The interpolation operator  $I_{k-1}^k$  maps  $(k-1)$ -level functions to  $k$ -level functions. Here, the coarse values are simply transferred to the four nearby fine grid points, i.e.,  $v_k(x_i, y_j) = I_{k-1}^k v_{k-1}(x_i, y_j) = v_{k-1}(x_i + \frac{h}{2}, y_j + \frac{h}{2})$  for  $i$  and  $j$  odd-numbered integers. The values at the other node points are given by

$$v_k(x_i + h, y_j) = v_k(x_i, y_j + h) = v_k(x_i + h, y_j + h) = v_{k-1}\left(x_i + \frac{h}{2}, y_j + \frac{h}{2}\right),$$

where  $i$  and  $j$  are odd.

(8) Compute the corrected approximation on  $\Omega_k$

$$c_k^{m, \text{after CGC}} = \bar{c}_k^m + \hat{v}_{1_k}^m, \quad \mu_k^{m-\frac{1}{2}, \text{after CGC}} = \bar{\mu}_k^{m-\frac{1}{2}} + \hat{v}_{2_k}^{m-\frac{1}{2}}.$$

(9) Postsmoothing

Compute  $\{c_k^{m+1}, \mu_k^{m+\frac{1}{2}}\}$  by applying  $v$  smoothing steps to  $c_k^{m, \text{after CGC}}, \mu_k^{m-\frac{1}{2}, \text{after CGC}}$

$$\{c_k^{m+1}, \mu_k^{m+\frac{1}{2}}\} = \text{SMOOTH}^v(c_k^n, c_k^{m, \text{after CGC}}, \mu_k^{m-\frac{1}{2}, \text{after CGC}}, \text{NSO}_k, f_k^n, g_k^n).$$

This completes the description of a nonlinear FAScycle. We next turn to the solution of the discrete system in the presence of flow.

### 5. Solution of system in presence of flow

Here, we present an iterative projection method for solving the coupled discrete NSCH system (14)–(17) and (18), (19). For simplicity, we focus on the case in which  $\eta$  is constant. Let  $\mathbf{u}^{*,k+1}$  be an intermediate velocity field and satisfy the following system for the iteration number  $k \geq 0$ :

$$\frac{\mathbf{u}^{*,k+1} - \mathbf{u}^n}{\Delta t} + \omega^{n+\frac{1}{2},k} \times \mathbf{u}^{n+\frac{1}{2},k} = -\tilde{\nabla}_d^c P^{n+\frac{1}{2},k} + \delta^k \mathbf{u}^{n+\frac{1}{2},k} + \frac{1}{2Re} \Delta_d (\mathbf{u}^{*,k+1} + \mathbf{u}^n) - \frac{We_s^{-1}}{\epsilon} c^{n+\frac{1}{2},k} \nabla_d \mu^{n+\frac{1}{2},k}, \quad (34)$$

where

$$\omega_{ij}^{n+\frac{1}{2},k} \times \mathbf{u}_{ij}^{n+\frac{1}{2},k} = \left( -\frac{\bar{v}_{i+1,j} - \bar{v}_{i-1,j} - \bar{u}_{i,j+1} + \bar{u}_{i,j-1}}{2h} \bar{v}_{ij}, \frac{\bar{v}_{i+1,j} - \bar{v}_{i-1,j} - \bar{u}_{i,j+1} + \bar{u}_{i,j-1}}{2h} \bar{u}_{ij} \right),$$

and

$$\delta^k = (\mathbf{u}^{n+\frac{1}{2},k}, \nabla_d^c P^{n+\frac{1}{2},k})_h / \|\mathbf{u}^{n+\frac{1}{2},k}\|^2 \quad (35)$$

and  $(\bar{\mathbf{u}}, \bar{\mathbf{v}}) = \mathbf{u}^{n+\frac{1}{2},k} \equiv (\mathbf{u}^{n+1,k} + \mathbf{u}^n)/2$  and  $c^{n+\frac{1}{2},k}$  is defined analogously. In the first step of the iteration, we take  $\mathbf{u}^{n+1,0} = \mathbf{u}^n$  and  $p^{n+\frac{1}{2},0} = p^{n-\frac{1}{2}}$ . Note that the pressure gradient, advection and surface force terms are treated as forcing functions. The fact that the latter two terms are treated in this way ensures, from Lemma 6, that the discrete system has an energy functional as  $k \rightarrow \infty$ , assuming that the iteration converges. Numerically, we found convergence is typically achieved in just two or three iterations. We are also investigating other algorithms for which the CH and NS equations are solved simultaneously. Following [27,28,53], Eq. (34) is solved for  $\mathbf{u}^{*,k+1}$  using a linear multigrid method.

The velocity field  $\mathbf{u}^{*,k+1}$  is not, in general, divergence-free. The projection step of the algorithm decomposes the intermediate velocity into a discrete gradient of a scalar potential and an approximately divergence-free vector field. They correspond to the pressure gradient and to the velocity updates, respectively. In particular, if  $\mathbf{P}$  represents the projection operator, then

$$\frac{\mathbf{u}^{n+1,k+1} - \mathbf{u}^n}{\Delta t} = \mathbf{P} \left( \frac{\mathbf{u}^{*,k+1} - \mathbf{u}^n}{\Delta t} \right) \equiv \frac{\mathbf{u}^{*,k+1} - \mathbf{u}^n}{\Delta t} - \tilde{\nabla}_d^c \psi, \quad (36)$$

where  $\psi$  is obtained by

$$\Delta_d^c \psi = \nabla_d^c \cdot \left( \frac{\mathbf{u}^{*,k+1} - \mathbf{u}^n}{\Delta t} \right), \quad (37)$$

with Neumann boundary conditions which are imposed by introducing a ring of ghost-cells surrounding the physical domain. Note that the velocity  $\mathbf{u}^{n+1,k+1}$  is only approximately divergence-free, i.e.,

$$\nabla_d^c \cdot \left( \frac{\mathbf{u}^{n+1,k+1} - \mathbf{u}^n}{\Delta t} \right) = \left( \Delta_d^c - \nabla_d^c \cdot \tilde{\nabla}_d^c \right) \psi. \quad (38)$$

The pressure is then updated using the second-order accurate scheme [25]:

$$p^{n+\frac{1}{2},k+1} = p^{n+\frac{1}{2},k} + \psi - \frac{\Delta t}{2Re} \Delta_d^c \psi. \quad (39)$$

We note that combining Eqs. (39) and (38) and letting  $k \rightarrow \infty$  (assuming that the iteration converges) yields Eq. (18) as claimed in Section 3. Analogously, plugging Eq. (36) into (34), and using Eq. (39), yields Eq. (19) also as claimed.

The approximate projection Poisson's equation (37) is solved using a linear multigrid method. Similar multigrid methods have been used in 3D [28] and in a finite element context in 2D [27].

In Section 6, we analyze the projection algorithm and demonstrate that the multigrid method convergence rate is insensitive to the grid size.

We next update the concentration field by

$$\frac{c^{n+1,k+1} - c^n}{\Delta t} + \nabla_d \cdot \left( \mathbf{u}^{n+\frac{1}{2},k+1} c^{n+\frac{1}{2},k} \right) = \Delta_d \mu^{n+\frac{1}{2},k+1}, \quad (40)$$

$$\mu^{n+\frac{1}{2},k+1} = \hat{\phi}(c^n, c^{n+1,k+1}) - \frac{\epsilon^2}{2} \Delta_d (c^n + c^{n+1,k+1}). \quad (41)$$

This system is solved using the non-linear multigrid method presented in Section 4 where the source term  $f^n$  is modified to account for the advection.

The above system (34)–(36) and (40), (41) is iterated in  $k$  until the difference between successive iterates is less than an error tolerance. As mentioned above, typically only two or three iterations are required to achieve an error tolerance of  $10^{-7}$ . We found that this number is insensitive to the value of the Weber number.

## 6. Local Fourier analysis

### 6.1. Absence of flow

To analyze the behavior of the multigrid method, we linearize the nonlinear scheme and perform a local Fourier analysis (e.g., see [53]). In particular, we analyze the smoother since the performance of the multigrid method depends strongly on the smoother.

Let  $c_{ij}^{n+1}, \mu_{ij}^{n+1}$  be the solution of the nonlinear discrete CH system (13) and (14). After linearizing the nonlinear term  $\hat{\phi}(c_{ij}^n, c_{ij}^{n+1}) = \frac{\alpha}{2}(c_{ij}^n + c_{ij}^{n+1}) + \beta$ , where  $\alpha = \phi'(c_m)$ ,  $c_m$  is an average concentration, and  $\beta$  is a constant and substituting  $\mu_{ij}^{n+1}$  into (13), the scheme becomes

$$L_h c_h^{n+1} = f_h^n,$$

where

$$L_h c_h^{n+1} := \frac{c_{ij}^{n+1}}{\Delta t} - \frac{\alpha}{2h^2} \left( c_{i-1,j}^{n+1} + c_{i+1,j}^{n+1} - 4c_{ij}^{n+1} + c_{i,j-1}^{n+1} + c_{i,j+1}^{n+1} \right) + \frac{\epsilon^2}{2h^4} \left[ c_{i-2,j}^{n+1} + c_{i+2,j}^{n+1} + c_{i,j-2}^{n+1} + c_{i,j+2}^{n+1} \right. \\ \left. + 2 \left( c_{i-1,j+1}^{n+1} + c_{i+1,j+1}^{n+1} + c_{i-1,j-1}^{n+1} + c_{i+1,j-1}^{n+1} \right) - 8 \left( c_{i-1,j}^{n+1} + c_{i+1,j}^{n+1} + c_{i,j-1}^{n+1} + c_{i,j+1}^{n+1} \right) + 20c_{ij}^{n+1} \right]$$

and

$$f_h^n = \frac{\alpha}{2} \Delta_d c_{ij}^n - \frac{\epsilon^2}{2} \Delta_d^2 c_{ij}^n + \frac{c_{ij}^n}{\Delta t}.$$

For Gauss–Seidel iteration with a lexicographic ordering of the grid points applied to the above equation, we have the following operator decomposition:

$$L_h^+ c_h^{n+1} := \frac{c_{ij}^{n+1}}{\Delta t} - \frac{\alpha}{2h^2} \left( c_{i-1,j}^{n+1} + c_{i,j-1}^{n+1} - 4c_{ij}^{n+1} \right) + \frac{\epsilon^2}{2h^4} \left[ c_{i-2,j}^{n+1} + c_{i,j-2}^{n+1} + 2 \left( c_{i-1,j+1}^{n+1} + c_{i-1,j-1}^{n+1} \right) \right. \\ \left. - 8 \left( c_{i-1,j}^{n+1} + c_{i,j-1}^{n+1} \right) + 20c_{ij}^{n+1} \right],$$



$$L_h^- c_h^{n+1} := -\frac{\alpha}{2h^2} (c_{i+1,j}^{n+1} + c_{i,j+1}^{n+1}) + \frac{\epsilon^2}{2h^4} [c_{i+2,j}^{n+1} + c_{i,j+2}^{n+1} + 2(c_{i+1,j+1}^{n+1} + c_{i+1,j-1}^{n+1}) - 8(c_{i+1,j}^{n+1} + c_{i,j+1}^{n+1})].$$

Therefore, this relaxation method (which is the linear analogue of the nonlinear multigrid smoother) can be written *locally* as

$$L_h^+ \tilde{z}_h + L_h^- z_h = f_h^n, \quad (42)$$

where  $z_h$  corresponds to the old approximation of  $c_h$  (approximation before the relaxation step) and  $\tilde{z}_h$  to the new approximation (after the step). Subtracting (42) from the discrete equation  $L_h c_h = f_h$  and letting  $\tilde{v}_h = c_h - \tilde{z}_h$  and  $v_h = c_h - z_h$ , we obtain the equation

$$L_h^+ \tilde{v}_h + L_h^- v_h = 0,$$

or, equivalently,

$$\tilde{v}_h = S_h v_h,$$

where  $S_h = -(L_h^+)^{-1} L_h^-$  is the resulting smoothing operator. Applying  $L_h^+$  and  $L_h^-$  to the formal eigenfunctions  $e^{i\theta_1 x/h} e^{i\theta_2 y/h}$ , we obtain

$$\begin{aligned} L_h^+ e^{i\theta_1 x/h} e^{i\theta_2 y/h} &= \hat{L}_h^+ e^{i\theta_1 x/h} e^{i\theta_2 y/h}, \\ L_h^- e^{i\theta_1 x/h} e^{i\theta_2 y/h} &= \hat{L}_h^- e^{i\theta_1 x/h} e^{i\theta_2 y/h}, \end{aligned}$$

where  $\hat{L}_h^+$  and  $\hat{L}_h^-$  are the symbols of the operators  $L_h^+$  and  $L_h^-$ , respectively:

$$\begin{aligned} \hat{L}_h^+(\theta_1, \theta_2) &= \frac{1}{\Delta t} - \frac{\alpha}{2h^2} (e^{-i\theta_1} + e^{-i\theta_2} - 4) + \frac{\epsilon^2}{2h^4} [e^{-2i\theta_1} + e^{-2i\theta_2} + 2(e^{-i(\theta_1-\theta_2)} + e^{-i(\theta_1+\theta_2)}) \\ &\quad - 8(e^{-i\theta_1} + e^{-i\theta_2}) + 20], \end{aligned}$$

$$\hat{L}_h^-(\theta_1, \theta_2) = -\frac{\alpha}{2h^2} (e^{i\theta_1} + e^{i\theta_2}) + \frac{\epsilon^2}{2h^4} [e^{2i\theta_1} + e^{2i\theta_2} + 2(e^{i(\theta_1+\theta_2)} + e^{i(\theta_1-\theta_2)}) - 8(e^{i\theta_1} + e^{i\theta_2})].$$

The amplification factor of the relaxation scheme is

$$\hat{S}_h(\theta_1, \theta_2) := -\frac{\hat{L}_h^-(\theta_1, \theta_2)}{\hat{L}_h^+(\theta_1, \theta_2)}.$$

Define the high frequency smoothing (HFS) factor:

$$\mu_{\text{loc}}(S_h) := \sup \left\{ |\hat{S}_h(\theta_1, \theta_2)| : \frac{\pi}{2} \leq |\theta_1|, |\theta_2| \leq \pi \right\}.$$

Here, as is typically done [53], we assume that the coarse grid operations are ideal and annihilate the low frequency error components while leaving the high frequency components unchanged. Therefore, we only consider  $\frac{\pi}{2} \leq |\theta_1|, |\theta_2| \leq \pi$ . We define a convergence factor as an average of the quantity  $\|d_h^m\|/\|d_h^{m-1}\|$ , where  $d_h^m$  ( $m = 1, 2, \dots$ ) are the defects.

The convergence factor is estimated numerically using our nonlinear code with the parameters  $\epsilon = 0.01$ , and the mesh-dependent time step  $\Delta t = 0.1h$  and initial conditions

$$c_0(x, y) = \begin{cases} 0.0 + 0.01 \cos(0.5\pi x/h) \cos(0.5\pi y/h), & \alpha = 0.5, \\ 0.5 + 0.01 \cos(0.5\pi x/h) \cos(0.5\pi y/h), & \alpha = -0.25. \end{cases}$$

We measure the  $V(m, n)$ -HFS factors, where  $m$  and  $n$  are the numbers of pre-smoothing and post-smoothing, with different mesh sizes. We focus on  $m = 1$  and  $n = 0$  and  $1$  as these yield the most efficient algorithms. In addition, we consider  $\alpha = 0.5$  and  $-0.25$ , where the positive (negative) values correspond to linearization in the stable (unstable, i.e., spinodal region) ranges of the evolution.

Table 1 shows HFS factors and measured  $V(m, n)$ -cycle convergence factors with different mesh sizes and  $\alpha = 0.5$ . Note  $\sqrt{V(1, 1)}$ -cycle means the square root of  $V(1, 1)$ -cycle convergence factor. Observe that with  $m = 1$  and  $n = 0$ , the HFS factor tends to 1 as the mesh is refined and thus suggests that the number of  $V$ -cycles required to solve the full system increases with increasing resolution. In fact this result is comparable to simply using Gauss–Siedel iteration without multigrid. However, the HFS factor corresponding to  $m = 1$  and  $n = 1$  remains uniformly bounded below 1 with increasing resolution and apparently converges to 0.4196 as  $h \rightarrow 0$ . This is significantly below the theoretical estimate 0.6693. Thus the number of  $V(1, 1)$ -cycles required to solve the full problem is insensitive to the resolution.

The HFS factors for  $\alpha = -0.25$  are given in Table 2. Their behavior is analogous to that observed for the  $\alpha = 0.5$ . Note that the HFS factor for  $V(1, 0)$ -cycles is actually greater than 1 at the finest resolution.

Together, these results for  $\alpha = 0.5$  and  $-0.25$  suggest that the multigrid method using a  $V(1, 1)$ -cycle with time step  $\Delta t \sim h$  converges uniformly with respect to increasing resolution. Correspondingly, this would impose a first-order time step constraint on our discrete scheme to solve the CH equation.

Next, let us consider results obtained using a *fixed*  $\Delta t = 0.005$  independent of the mesh size  $h$ . All other parameters are as before. This value of  $\Delta t$  roughly corresponds to that used in Tables 1 and 2 with  $h = 1/16$ . Table 3 shows the  $V(1, 1)$ -HFS factors with different mesh sizes and  $\alpha = 0.5$ . Again, the results are qualitatively similar to the case with variable  $\Delta t \sim h$ . When  $\alpha = -0.25$ , however, the results are very different. This is seen in Table 4. The numerical HFS factor now tends to 1 as the mesh is refined in spite of the fact that theoretical HFS factors are comparable for all choices of  $\Delta t$  and  $\alpha$ . This behavior at fine grids occurs because the coarse grid correction steps internal to the  $V$ -cycle use much larger time steps when  $\Delta t$  is fixed than when  $\Delta t \sim h$ , where  $h$  is the fine grid size. This can be seen in Figs. 1(left,right), where diagonal slices of the amplification factors  $|\hat{S}_h(\theta, \theta)|$ , for  $\theta \in [-\pi, \pi]$ , are shown for  $h = 1/16$ ,  $1/32$  and  $1/2048$ , where  $\Delta t = 0.005$  (left) and  $\Delta t = 0.1/2048$  (right). Observe that for the latter case, the amplification factors for the coarse meshes are nearly equal to zero in contrast to the case with the larger time step.

These results suggest that when a fixed  $\Delta t$  is used, its value should be such that the coarse grid HFS factors are less than 1. This is confirmed in Table 5 where the HFS factors are shown with  $\Delta t = 0.1/64 = 1.5625 \times 10^{-3}$ . This suggests that the multigrid method using a  $V(1, 1)$ -cycle with fixed time step  $\Delta t$  converges uniformly with respect to increasing resolution if  $\Delta t$  is small enough. This would impose no grid-dependent time step constraints on our discrete scheme to solve the CH equation.

Table 1  
HFS factors for different mesh sizes.  $\alpha = 0.5$ ,  $\Delta t = 0.1h$  and  $h = 1/N$

Case	$16 \times 16$	$32 \times 32$	$64 \times 64$	$128 \times 128$
$\mu_{\text{loc}}$	0.1493	0.1581	0.4570	0.6092
$V(1, 0)$ -cycle	0.1643	0.2108	0.2865	0.3489
$\sqrt{V(1, 1)}$ -cycle	0.2108	0.2462	0.2840	0.3434
Case	$256 \times 256$	$512 \times 512$	$1024 \times 1024$	$2048 \times 2048$
$\mu_{\text{loc}}$	0.6541	0.6657	0.6686	0.6693
$V(1, 0)$ -cycle	0.4636	0.6563	0.8198	0.9810
$\sqrt{V(1, 1)}$ -cycle	0.4021	0.4171	0.4196	0.4196

Table 2

HFS factors for different mesh sizes.  $\alpha = -0.25$ ,  $\Delta t = 0.1h$  and  $h = 1/N$ 

Case	$16 \times 16$	$32 \times 32$	$64 \times 64$	$128 \times 128$
$\mu_{\text{loc}}$	1.3773	1.1563	0.7874	0.6992
$V(1,0)$ -cycle	0.5183	0.5837	0.4245	0.4829
$\sqrt{V(1,1)}$ -cycle	0.5501	0.6061	0.3706	0.4162
Case	$256 \times 256$	$512 \times 512$	$1024 \times 1024$	$2048 \times 2048$
$\mu_{\text{loc}}$	0.6771	0.6714	0.6700	0.6697
$V(1,0)$ -cycle	0.6260	0.7904	0.8719	N/A
$\sqrt{V(1,1)}$ -cycle	0.4141	0.4209	0.4299	0.4382

Table 3

HFS factors for different mesh sizes.  $\alpha = 0.5$  and  $\Delta t = 5 \times 10^{-3}$ 

Case	$16 \times 16$	$32 \times 32$	$64 \times 64$	$128 \times 128$
$\mu_{\text{loc}}$	0.1390	0.1629	0.4634	0.6106
$\sqrt{V(1,1)}$ -cycle	0.1930	0.2706	0.3428	0.3920
Case	$256 \times 256$	$512 \times 512$	$1024 \times 1024$	$2048 \times 2048$
$\mu_{\text{loc}}$	0.6543	0.6657	0.6686	0.6693
$\sqrt{V(1,1)}$ -cycle	0.4127	0.4199	0.4294	0.4452

Table 4

HFS factors for different mesh sizes.  $\alpha = -0.25$  and  $\Delta t = 5 \times 10^{-3}$ 

Case	$16 \times 16$	$32 \times 32$	$64 \times 64$	$128 \times 128$
$\mu_{\text{loc}}$	0.9594	1.2796	0.8014	0.7009
$\sqrt{V(1,1)}$ -cycle	0.3925	0.8503	0.9098	0.9177
Case	$256 \times 256$	$512 \times 512$	$1024 \times 1024$	$2048 \times 2048$
$\mu_{\text{loc}}$	0.6773	0.6715	0.6700	0.6697
$\sqrt{V(1,1)}$ -cycle	0.9209	0.9220	0.9208	0.9860

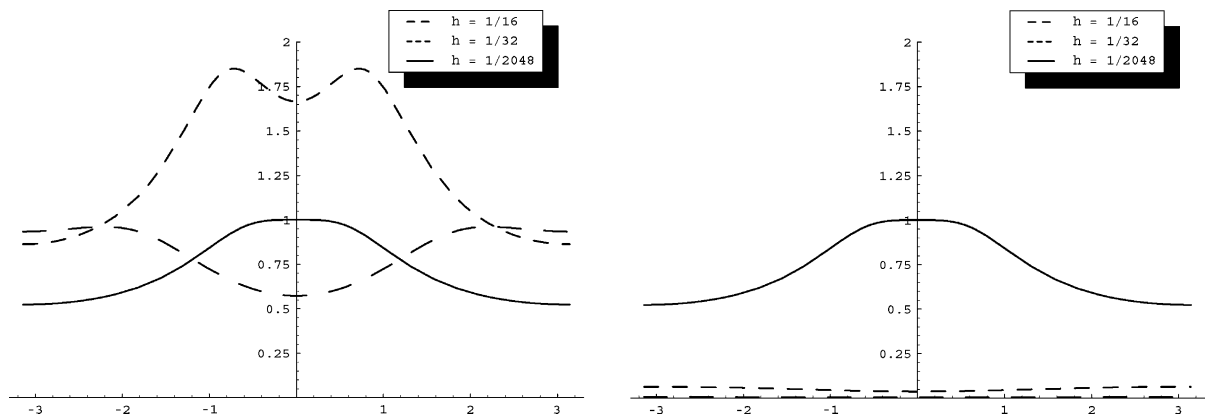
Fig. 1. Diagonal slice of amplification factor  $|\hat{S}_h(\theta, \theta)|$ , over the interval  $[-\pi, \pi]$ . In the left figure,  $\Delta t = 0.005$ . In the right figure,  $\Delta t = 0.1/2048$ .

Table 5

HFS factors for different mesh sizes.  $\alpha = -0.25$ ,  $\Delta t = .1/64 = 1.5625 \times 10^{-3}$ 

Case	$16 \times 16$	$32 \times 32$	$64 \times 64$	$128 \times 128$
$\mu_{\text{loc}}$	0.2324	0.9016	0.7874	0.7002
$\sqrt{V(1,1)}$ -cycle	0.1305	0.5117	0.3522	0.3907
Case	$256 \times 256$	$512 \times 512$	$1024 \times 1024$	$2048 \times 2048$
$\mu_{\text{loc}}$	0.6772	0.6715	0.6700	0.6697
$\sqrt{V(1,1)}$ -cycle	0.4228	0.4206	0.4290	0.4495

**Remark 9.** Numerical results (e.g., not shown here) also demonstrate that the HFS factors are insensitive to the value of  $\epsilon$  provided variations in  $c$  are resolved by the computational mesh. For example, 4 grid points seem to be sufficient to resolve a transition from  $c = 0.1$  to  $c = 0.9$ . Such a transition occurs over a layer of width  $4\sqrt{2}\epsilon$  during the later stages of phase-separation and the quartic free energy is used [4].

### 6.2. Presence of flow

Here, we analyze approximate projection algorithm given in Section 5 (an analysis of the multigrid method used to solve for the intermediate velocity is similar and thus is not presented). The multigrid smoothing operator  $L_h^{\text{approx}} = L_h^{a,+} + L_h^{a,-}$  where

$$L_h^{a,+} \psi := \left( \psi_{i+\frac{1}{2},j+\frac{3}{2}} - 4\psi_{i+\frac{1}{2},j+\frac{1}{2}} + \psi_{i+\frac{3}{2},j+\frac{1}{2}} \right) / h^2,$$

$$L_h^{a,-} \psi := \left( \psi_{i-\frac{1}{2},j+\frac{1}{2}} + \psi_{i+\frac{1}{2},j-\frac{1}{2}} \right) / h^2.$$

The resulting amplification factor is

$$\hat{S}_h^a(\theta_1, \theta_2) := -\frac{\hat{L}_h^{a,-}(\theta_1, \theta_2)}{\hat{L}_h^{a,+}(\theta_1, \theta_2)},$$

where the symbols are calculated as in Section 6.1. In Fig. 2 (left), the diagonal slice  $|\hat{S}_h^a(\theta, \theta)|$  is shown. Observe that the HFS factor  $\mu_{\text{loc}} \approx 0.45$  which suggests that the linear multigrid converges uniformly with respect to increasing resolution. For purposes of comparison, the corresponding amplification factor is

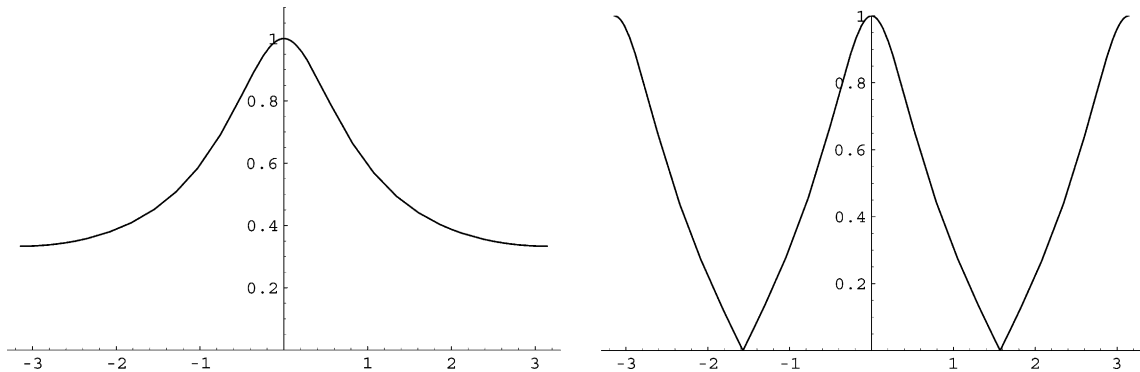


Fig. 2. Diagonal slices of amplification factor. Approximate projection (left), exact projection (right).

shown (right) for the exact projection method (i.e., where  $\Delta_d^c \equiv \nabla_d^c \cdot \tilde{\nabla}_d^c$ ). In the case of exact projection, however, the HFS factor  $\mu_{\text{loc}} \approx 1.0$  and suggests that the smoothing operator does not remove high frequencies efficiently which reflects the ill-conditioning of the system. The corresponding multigrid method requires a prohibitive number of iterations to converge when the mesh size  $h$  is small. This is why the approximate projection algorithm is used (see also [49]).

## 7. Numerical experiments

In this section, we validate our scheme by verifying the second-order convergence and comparing the numerical results with the prediction of a linear stability analysis. We then perform simulations of spinodal decomposition and examine the effect of boundary conditions, flow and interfacial tension.

### 7.1. Convergence test

To obtain an estimate of the rate of convergence, we perform a number of simulations for a sample initial problem on a set of increasingly finer grids. We begin by considering the case in the absence of flow ( $\mathbf{u} = \mathbf{0}$ ). The initial data is

$$c_0(x, y) = 0.5 + 0.12 \cos(2\pi x) \cos(2\pi y) + 0.2 \cos(\pi x) \cos(3\pi y) \quad (43)$$

on a square domain,  $[0, 1] \times [0, 1]$ . The numerical solutions are computed on the uniform grids,  $\Delta x = \Delta y = h = 1/2^n$  for  $n = 5$  to 9. For each case, the convergence is measured at time  $t = 0.2$ , the uniform time steps,  $\Delta t = 0.1h$  and  $\epsilon = 0.01$ , are used to establish the convergence rates.

In our formulation of the method for the CH equation, since a cell centered grid is used, we define the error to be the discrete  $L_2$ -norm of the difference between that grid and the average of the next finer grid cells covering it:

$$e_{h/\frac{h}{2}} \stackrel{\text{def}}{=} c_{hij} - \left( c_{\frac{h}{2}2i,2j} + c_{\frac{h}{2}2i-1,2j} + c_{\frac{h}{2}2i,2j-1} + c_{\frac{h}{2}2i-1,2j-1} \right) / 4.$$

The rate of convergence is defined as the ratio of successive errors:

$$\log_2(\|e_{h/\frac{h}{2}}\| / \|e_{\frac{h}{2}}\|).$$

The errors and rates of convergence are given in Table 6. The results suggest that the scheme is indeed second-order accurate. The deterioration of the rates from 2 at higher resolutions is believed to be due to accumulation of errors from coarse grid correction steps internal to the nonlinear multigrid method. In Fig. 3, the time evolution of the energy is shown accompanied with grey-scale contour images of the numerical solution  $c$  at the (filled) levels from 0 to 0.25 (black), 0.25 to 0.5, 0.5 to 0.75 and 0.75 to 1.0 (white). As expected from theorem (26), the energy is non-increasing and tends to a constant value. The concentration phase-separates and depletes the center region of the domain. The phase accumulates at the  $y$ -boundaries which then straighten to lower the energy and to subsequently form two horizontal bands. This is in fact a local equilibrium for Neumann boundary conditions. The global equilibrium consists of a single interface.

Table 6

$l_2$ -norm of the errors and convergence rates for concentration  $c$

Case	32–64	Rate	64–128	Rate	128–256	Rate	256–512
$l_2$	4.03e–02	3.29	4.12e–03	2.03	1.01e–03	1.96	2.60e–04

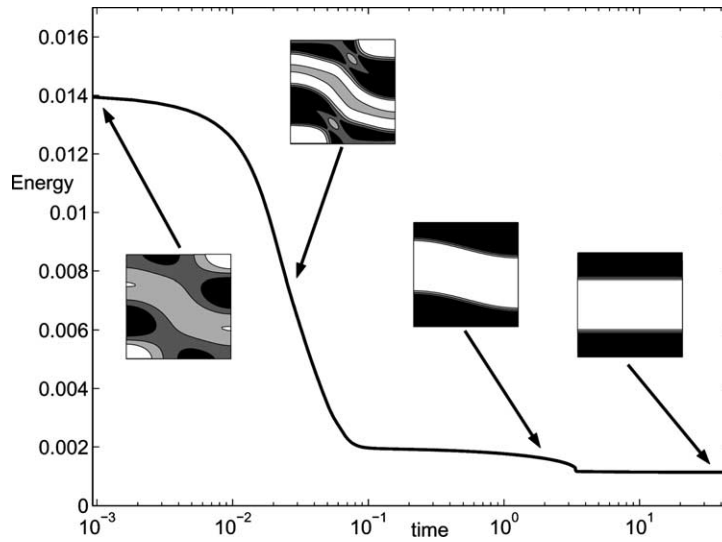


Fig. 3. The time dependent energy of the numerical solutions with the initial data (43). Snapshots of the concentration field are shown with filled contours at the three levels  $c = 0.25, 0.5$  and  $0.75$ .

Next, let us consider the convergence of the algorithm in the presence of flow. We take the same initial concentration as in Eq. (43) and the initial velocity is taken to be the rotation

$$u(x, y) = -\sin^2(\pi x) \sin(2\pi y), \quad v(x, y) = \sin^2(\pi y) \sin(2\pi x). \quad (44)$$

The viscosity  $\eta$  is constant and  $Re = 100$  and  $We_s = 100$ , which corresponds to the physical Weber number  $We = 848.5$ . No-slip boundary conditions are applied at the boundaries of the domain. The simulation parameters, convergence time and error measurement are as in the case without flow. In Table 7, the errors and rates of convergence are shown for the concentration  $c$  and the velocity components  $u$  and  $v$ , respectively. Observe that these quantities converge with second-order accuracy.

In Table 8, the errors and convergence rate for the pressure are shown. Here, the rate of convergence appears to be less than second order.

Finally, in Table 9, the values of  $\delta$  are shown. Observe that  $\delta$  converges to zero with second-order accuracy.

In Fig. 4, the time evolution of the energy is shown accompanied by the grey-scale contour images of the concentration field at the indicated times. The contour values shown are the same as in the case without flow. At early times, the phases separate and rotate about the center of the domain due to the fluid flow. Between  $t = 0.7$  and  $t = 1.0$ , the thin necks pinch off and the lower (upper) bulbs of fluid reconnect with the upper (lower) regions of fluid near the boundaries of the domain and a wiggly interface develops. Due to surface tension, the wiggles straighten out and the bulbs redevelop. At the same time, the rotation slows due

Table 7

$l_2$ -norm of the errors and convergence rates for concentration  $c$  and velocity  $(u, v)$

Case	32–64	Rate	64–128	Rate	128–256	Rate	256–512
$c$	6.03e–02	3.59	5.00e–03	2.06	1.20e–03	2.01	2.97e–04
$u$	1.10e–03	1.79	3.23e–04	1.99	8.13e–05	2.00	2.04e–05
$v$	1.20e–03	1.83	3.24e–04	1.99	8.16e–05	2.00	2.05e–05

Table 8

 $l_2$ -norm of the errors and convergence rates for pressure  $p$ 

Case	33–65	Rate	65–129	Rate	129–257	Rate	257–513
$l_2$	$2.40\text{e}-03$	2.92	$3.13\text{e}-04$	1.77	$9.15\text{e}-05$	1.55	$3.13\text{e}-05$

Table 9

Values of  $\delta$  and convergence rate

Case	64	Rate	128	Rate	256	Rate	512
$\delta$	$-4.40\text{e}-04$	1.98	$-1.11\text{e}-04$	2.00	$-2.80\text{e}-05$	1.99	$-7.04\text{e}-06$

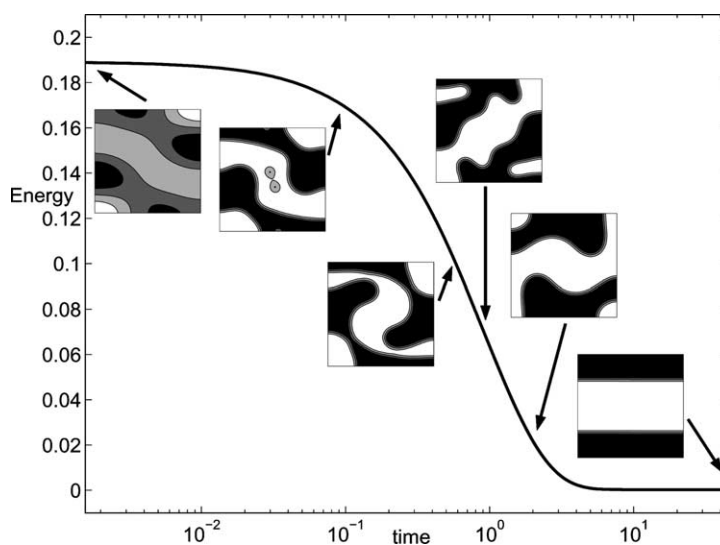


Fig. 4. The time dependent total energy of the numerical solutions with the initial data (43).

to viscous dissipation. The regions of fluid then further straighten, again due to surface tension, to form two horizontal bands. This is the same local equilibrium structure that develops in the case without flow even though the dynamics is very different. However, here the bands consist of fluid originating in both the upper and lower regions of the box while in the case without flow, the fluid in the bands originates from the same region of the box as the band. Observe that the total energy decreases to a constant value consistent with Theorem 6.

## 7.2. Comparison with linear stability theory

Next, to ensure that we are simulating the correct physical problem, we consider the agreement between the numerics and the results of a linear stability analysis about a constant concentration  $c = c_m$  and velocity  $\mathbf{u} = \mathbf{0}$ . Accordingly, we look for a solution of equation (1) of the form

$$c(x, t) = c_m + \sum_{k=1}^{\infty} c^k(t) \cos(k\pi x),$$

where  $|c^k(t)| \ll 1$ . Neglecting quadratic terms in  $c^k(t)$ , we find that  $c^k(t)$  must solve the ordinary differential equation,

$$\frac{dc^k}{dt} = -(k\pi)^2[\phi'(c_m) + \epsilon^2(k\pi)^2]c^k. \quad (45)$$

Note that there is no flow at the linear level since at that level the pressure balances the extra-stress coupling term in the Navier–Stokes equation. The solution of Eq. (45) is  $c^k(t) = c^k(0)e^{\eta_k t}$ , where  $\eta_k = -(k\pi)^2(\phi'(c_m) + \epsilon^2(k\pi)^2)$  is the growth rate. Taking  $c_m$  in the spinodal region (i.e.,  $c_m \in (\frac{3-\sqrt{3}}{6}, \frac{3+\sqrt{3}}{6})$ ,  $\phi'(c_m) < 0$ ), Eq. (45) shows that the amplitude of a finite number of long wavelength perturbations will grow exponentially in time for sufficiently small  $\epsilon$ . In particular the fastest growing mode is

$$k_{\max} = \sqrt{-\phi'(c_m)/(2\epsilon^2\pi^2)},$$

and the growth rate of this mode is  $\eta_{k_{\max}} = -(k_{\max}\pi)^2\phi'(c_m)/2$ .

In Fig. 5, the theoretical growth rate  $\eta_k$  is compared to that obtained from the nonlinear scheme. The numerical growth rate is defined by

$$\tilde{\eta}_k = \log \left( \frac{\max_{i,j} |c_{i,j}^n - 0.5|}{\max_{i,j} |c_{i,j}^0 - 0.5|} \right) / t_n.$$

Here, we used  $c_m = 0.5$ , initial data  $c_0(x) = 0.5 + 0.01 \cos(k\pi x)$  and  $\epsilon = 0.018757$ ,  $\Delta t = 10^{-4}$ ,  $h = 1/128$  and  $t_n = 0.01$ . The graph shows that the linear analysis (solid line) and numerical solution (circle) are in good agreement.

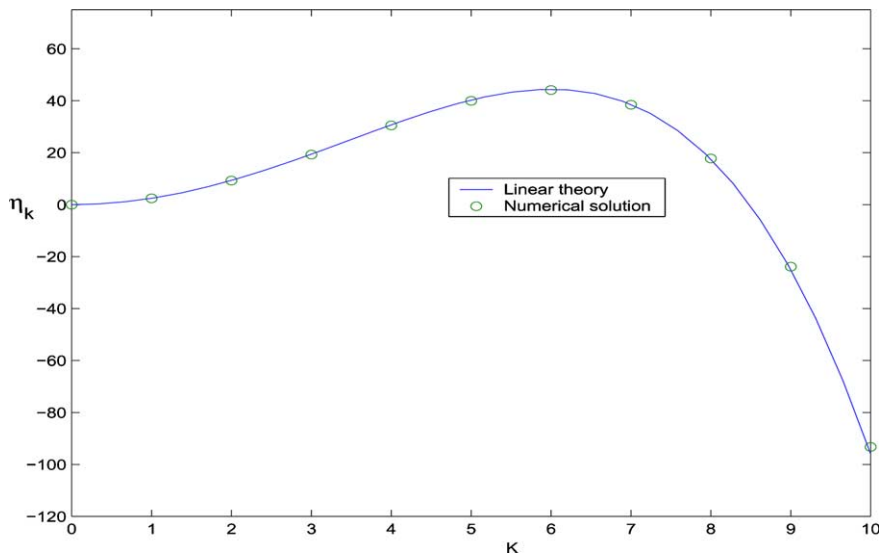


Fig. 5. Growth rate for the different wave numbers  $k$ .



### 7.3. Spinodal decomposition

In order to demonstrate the effectiveness of our new numerical scheme we consider the effect of flow on spinodal decomposition [26]. We consider an initial concentration field  $c^0(\mathbf{x}) = c_m + \xi(\mathbf{x})$ , where  $c_m = 0.5$  is the spinodal point and  $\xi(\mathbf{x})$  is a random perturbation with magnitude  $|\xi(\mathbf{x})| \leq 0.01$ . A  $64 \times 64$  mesh was used on the square  $\Omega = [0, 1] \times [0, 1]$  with periodic boundary conditions at  $x = 0$  and  $1$ . On  $y = 0$  and  $1$  we used either no-slip velocity boundary conditions or an imposed shear. Neumann boundary conditions are used for  $c$  and  $\mu$ . Further, we took  $\epsilon = 0.01$ ,  $h = 1/64$ , and  $\Delta t = 0.1h$ . In Fig. 6, the evolution is shown with no flow (left column) and in the presence of surface tension driven flow (right column) with  $We_s = 6\sqrt{2}$  (this corresponds to the physical Weber number  $We = 1$ ). That is, the flow arises only due to surface stresses between the components and we have taken  $Re = 1$  and the viscosity  $\eta$  is constant. In Fig. 7, the evolution is shown in the absence and presence of surface stress (left and right columns, respectively) and with an imposed shear flow, i.e.,  $(u(x, 1), v(x, 1)) = (\frac{1}{2}, 0)$  and  $(u(x, 0), v(x, 0)) = (-\frac{1}{2}, 0)$ . In the absence of surface stress, the velocity is the linear field  $(u(x, y), v(x, y)) = (y - 1/2, 0)$  and satisfies the Navier–Stokes equation (7) with  $We_s = \infty$ . In the presence of surface stress, the velocity field is non-linear and we have again used the same non-dimensional constants as given above.

In Figs. 6 and 7, three spatial periods are shown, the  $c = 0.25, 0.5$  and  $0.75$  contours are shown as filled as before, and the time is constant across a row and increases down the column as indicated in the caption. The times in the corresponding rows for Figs. 6 and 7 are the same. At early times, there is classical spinodal decomposition as the unstable mixture phase separates and regions coalesce. There is little effect of surface stress and flow.

Let us focus first on the effect of surface tension in the absence of shear. In Fig. 6, at later times, we observe that surface tension acts to decrease the deformation of the interfaces and to reduce their overall length. This causes the fluid fingers to retract and become more vertical. This leads to the coalescence of the fingers with semi-circular drops at the bottom of the domain. The resulting vertical bands of fluid are a local equilibrium. In the absence of surface tension, the fingers do not coalesce with the drops and classical coarsening occurs as the mass transfers from the drops to the fingers. The fingers then coalesce to form a horizontal band. This is a global energy minimum.

In the presence of shear, we see from Fig. 7, that surface tension has a similar effect and the deformation of interfaces is reduced. Here, however, the morphologies are much more elongated due to the shear. Further, pinchoff and reconnection events occur and the morphology actually repeats itself in time. The stretched bands at  $t = 5.63$  pinchoff and form drops (see  $t = 6.56$ ). The drops then reconnect with the fingers (approximately at  $t = 7.0$ , not shown) and re-form the stretched bands. When  $We_s = \infty$ , this sequence occurs twice while when  $We_s = 6\sqrt{2}$  this sequence occurs three times since the fingers retract more due to surface tension which enhances their capability to coalesce. This temporal periodicity is discussed further below. Eventually, the periodicity is broken since the drops that are formed become smaller with each cycle. After the last cycle, there is no reconnection. The fingers then merge to form a single horizontal band which is the global energy minimum.

In Fig. 8 the total energy (27) evolution for the different simulations is plotted versus time. In the absence of shear (dot-dashed:  $We_s = 6\sqrt{2}$  and dashed:  $We_s = \infty$ ), the energy decreases monotonically as predicted by Theorem 6. In the presence of shear (large dots:  $We_s = 6\sqrt{2}$  and small dots:  $We_s = \infty$ ), there are energy oscillations. Observe that there are three oscillations when  $We_s = 6\sqrt{2}$  and two when  $We_s = \infty$ . These correspond to the pinchoff and reconnection scenarios described above.

In Fig. 9, we present the scaled kinetic (dashed) and surface energy (solid) evolutions through first oscillation ending approximately at  $t = 9.0$ . In addition, we show the concentration morphology at the indicated times. To obtain the scaled kinetic energy, the actual kinetic energy is multiplied by 100. At early times, energy is transferred from the surface to the fluid while at later times this process is reversed as the

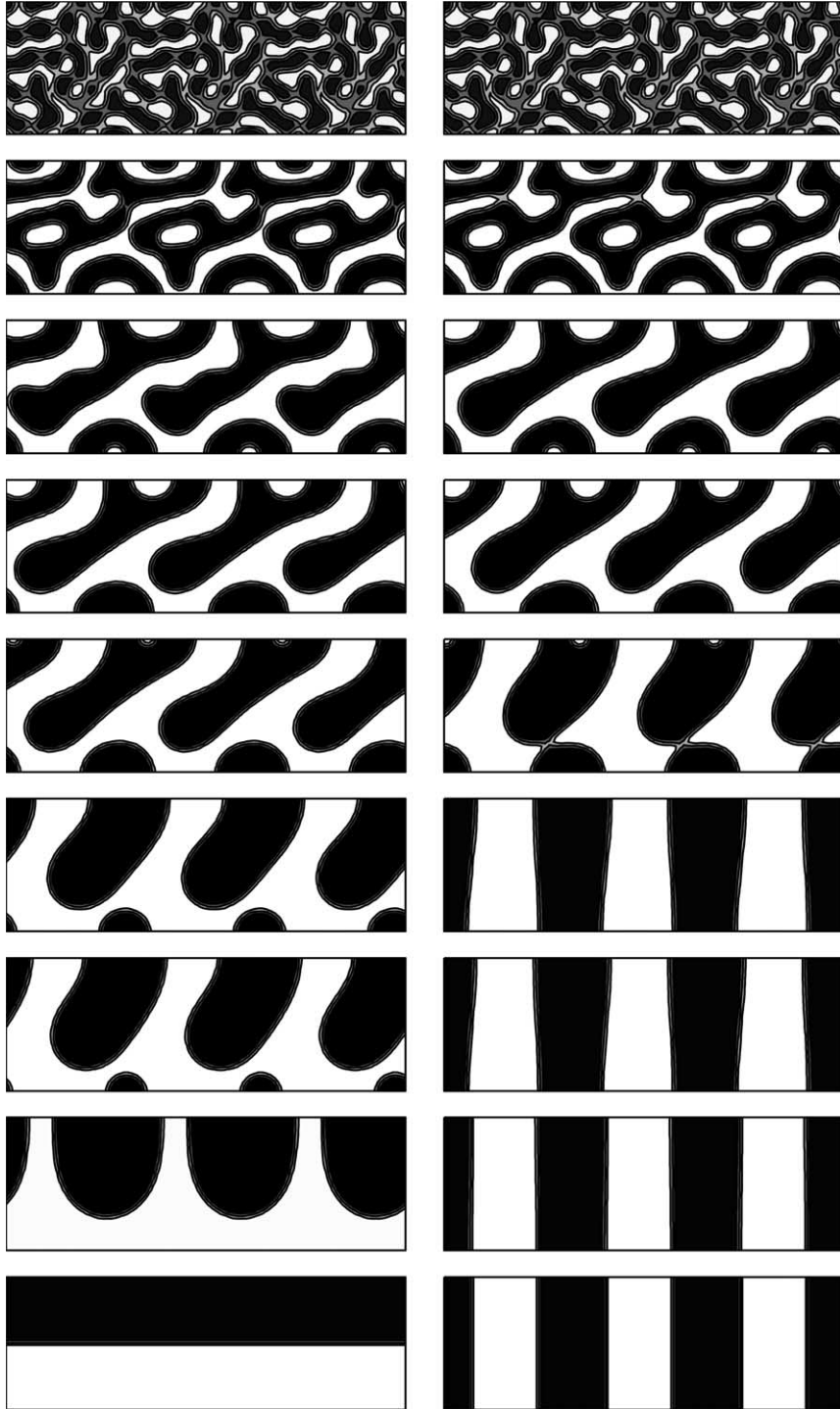


Fig. 6. Evolution with  $We_s = \infty$  (left column) and  $We_s = 6\sqrt{2}$  (right column). No applied shear. The times shown are (from top to bottom)  $t = 0.03, 0.16, 0.56, 0.94, 1.88, 5.63, 6.56, 17.81$  and  $45.94$ .

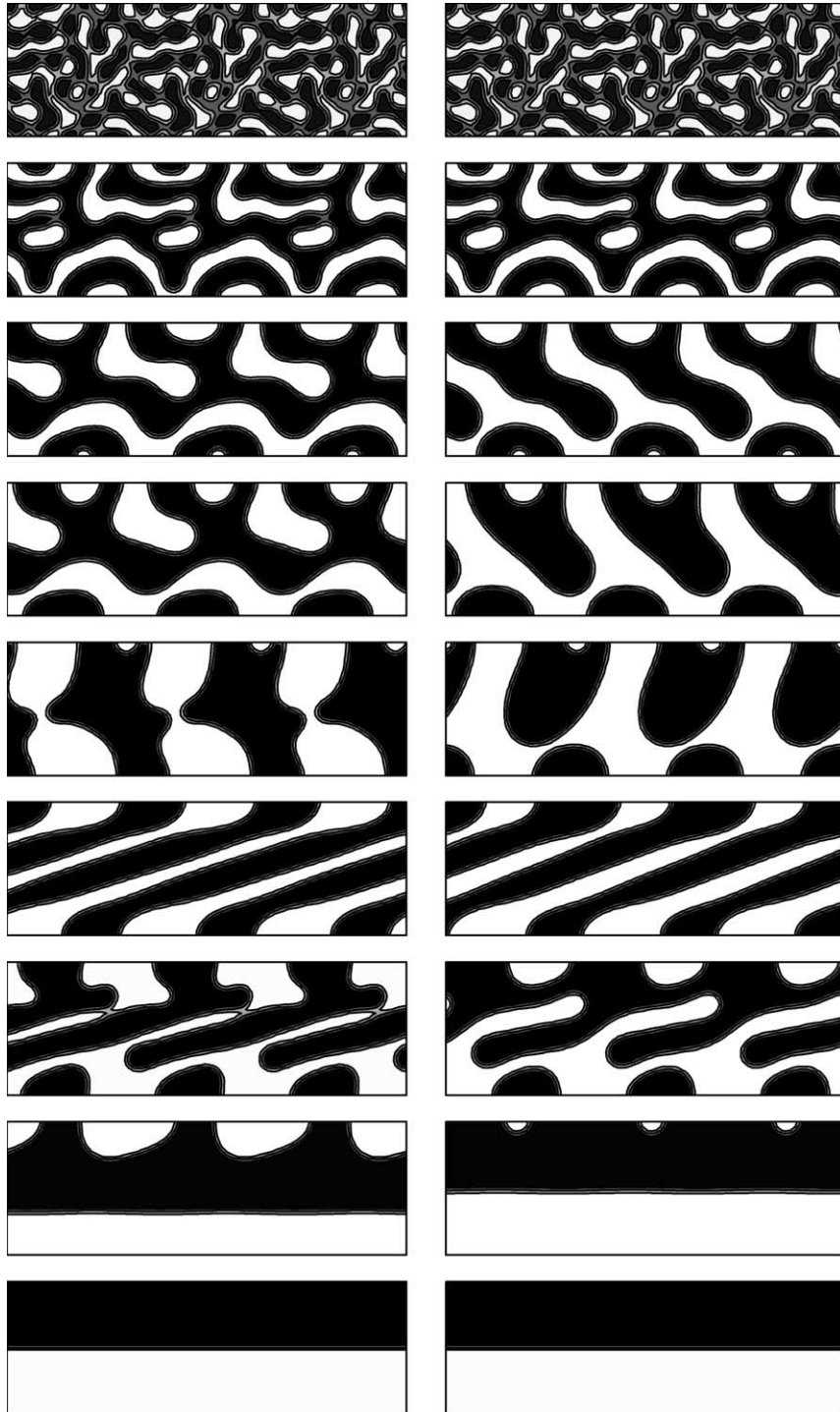


Fig. 7. Evolution with  $We_s = \infty$  (left column) and  $We_s = 6\sqrt{2}$  (right column). Applied shear conditions. The times shown are identical to those in Fig. 6.

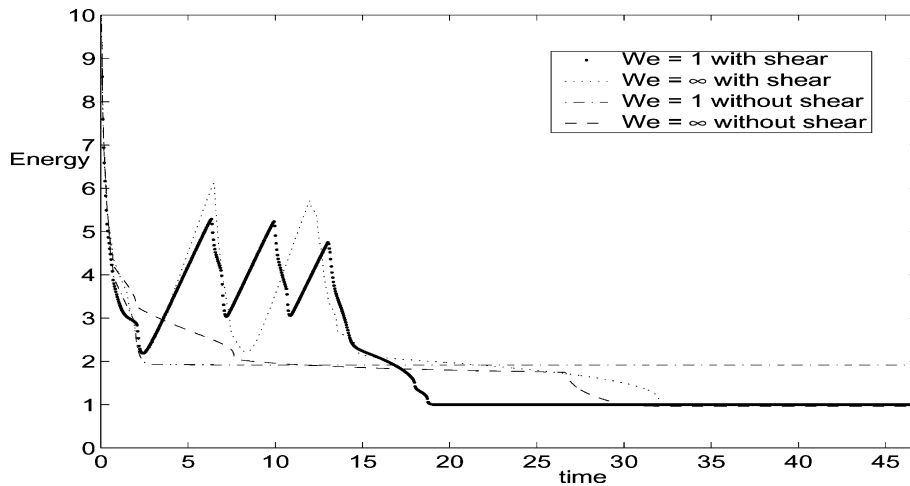


Fig. 8. Energy evolution under the flow different conditions.

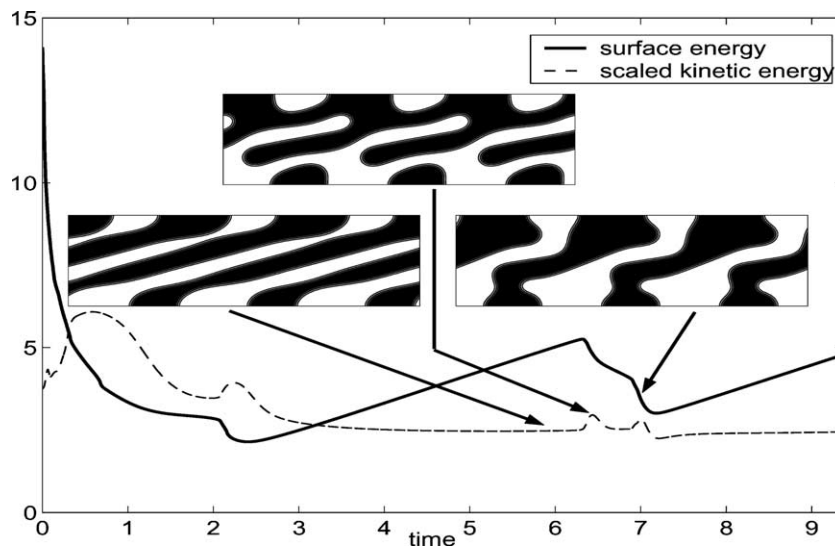


Fig. 9. Surface energy and scaled kinetic energy.

interfaces stretch and elongate. The peaks seen in the kinetic energy correspond to topology transitions of the concentration field in the flow. For example, lower ends of the stretched bands pinchoff to form drops at approximately  $t = 6.4$ . The drops then recombine with the fingers at approximately  $t = 7.0$ . Each of these events is seen to be associated with a local peak in the kinetic energy. Energy is transmitted to the fluid through the large surface stress that develops during the transition and subsequent retraction of the fingers.

To understand further the oscillation of the energy in the presence of shear, we compare in Fig. 10 the difference quotient

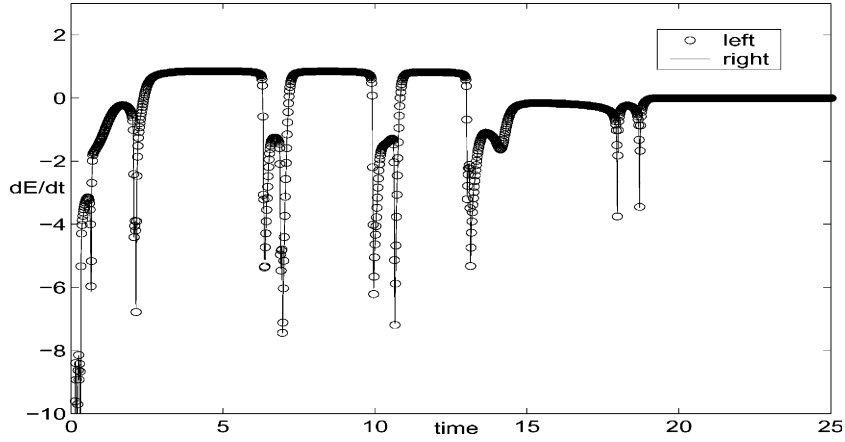


Fig. 10. Comparison of Eqs. (46), circles, and (47), solid line.

$$\frac{\mathcal{E}_h(c^{n+1}, \mathbf{u}^{n+1}) - \mathcal{E}_h(c^n, \mathbf{u}^n)}{\Delta t} \quad (46)$$

shown as circles to the corresponding spatial discretization of the analytical value  $\frac{d}{dt} \mathcal{E}(c^{n+\frac{1}{2}}, \mathbf{u}^{n+\frac{1}{2}})$  given by

$$\frac{1}{Re} (\mathbf{u}^{n+\frac{1}{2}}, \Delta \mathbf{u}^{n+\frac{1}{2}})_h - \frac{We_s^{-1}}{\epsilon} (|\nabla \mu^{n+\frac{1}{2}}|^2, 1)_h - \frac{We_s^{-1}}{\epsilon \Delta t} ((c^{n+1} - c^n)^4, 1)_h \quad (47)$$

shown as the solid line. Observe that there is excellent agreement between these two independently calculated quantities. This shows that the oscillations are due to the flow through the shear boundary condition and provides an independent validation of the accuracy of our numerical results.

## 8. Conclusions

In this paper, we have developed a conservative, second-order accurate fully implicit discretization of the NSCH system that has an associated discrete energy functional. In addition, the scheme has a straightforward extension to multi-component systems. This is exploited in [3] where we examine fluid flows with three constituent components.

To efficiently solve the discrete system at the implicit time-level, we have developed a nonlinear multigrid method to solve the CH equation which is then coupled to a projection method that is used to solve the NS equation. We demonstrated convergence of our scheme numerically in both the presence and absence of flow and performed simulations of phase separation via spinodal decomposition. We examined the separate effects of surface tension and external flow on the decomposition. We found surface tension driven flow alone increases coalescence rates through the retraction of interfaces. When there is an external shear flow, the evolution of the flow is nontrivial and the flow morphology repeats itself in time as multiple pinchoff and reconnection events occur. Eventually, the periodic motion ceases and the system relaxes to a global equilibrium. The equilibria we observe appears has a similar structure in all cases although the dynamics of the evolution is quite different.

We view the work presented in this paper as preparatory for the detailed investigation of liquid–liquid interfaces with surface tension where the interfaces separate two immiscible fluids. In this situation, the interface layer has thickness  $4\sqrt{2}\epsilon$  using the quartic free energy [4]. Simulations suggest that 4 grid cells

are needed across the layer for accuracy and thus  $h \approx \sqrt{2}\epsilon$  is required. This is approximately the same condition relating the grid spacing and smoothing width used in a variety of level set and volume of fluid methods (e.g., see the reviews [55–57] and the references therein). To improve performance and increase efficiency, clearly adaptive mesh algorithms should be used. See for example [33] for an adaptive finite element algorithm for the CH equation and [58] for an adaptive finite difference method for level-set simulations of two-phase flows. We have also recently developed an adaptive remeshing algorithm for unstructured meshes [59] and performed simulations of interface transitions in multiphase flows using a finite-element level-set method. This adaptive algorithm will be used in the future with the NSCH system.

To demonstrate the potential of using the NSCH system to accurately describe complex multiphase flows, we present an example simulation of the break-up of an axisymmetric thread of viscous fluid surrounded by another liquid due to the Rayleigh instability. In Fig. 11, the break-up of such a thread is shown using an axisymmetric version of the NSCH algorithm presented in this paper using a nonconstant mobility  $M(c) = c(1 - c)$  [23]. In this simulation, the initial condition consists of a column of fluid with radius  $r_0 = 0.5$  perturbed by a cosine perturbation with an amplitude of  $\alpha(0) = 0.025$ . The initial velocity is equal to zero. The inner and outer fluids have the same density and viscosity. The Reynolds number (using the characteristic velocity scale that is proportional to the ratio of surface tension and viscosity and length scale that is proportional to the radius of the column) is  $Re = 0.125$ . The physical Weber number is  $We = 6.25 \times 10^{-3}$ , which corresponds to  $We_s = 7.37 \times 10^{-4}$ . The time step  $\Delta t = 1 \times 10^{-3}$ , the domain is  $0 \leq r \leq \pi$  and  $0 \leq z \leq 2\pi$ . The grid size is  $h = \pi/128 \approx 0.0245$  in both  $r$  and  $z$ . Periodic boundary conditions are imposed at  $z = 0$  and  $2\pi$ . Neumann and no-slip boundary conditions are imposed at  $r = \pi$  for  $c$ ,  $\mu$  and  $\mathbf{u}$ , respectively. Finally,  $\epsilon = 0.01$  and  $Pe = 10/\epsilon$ .

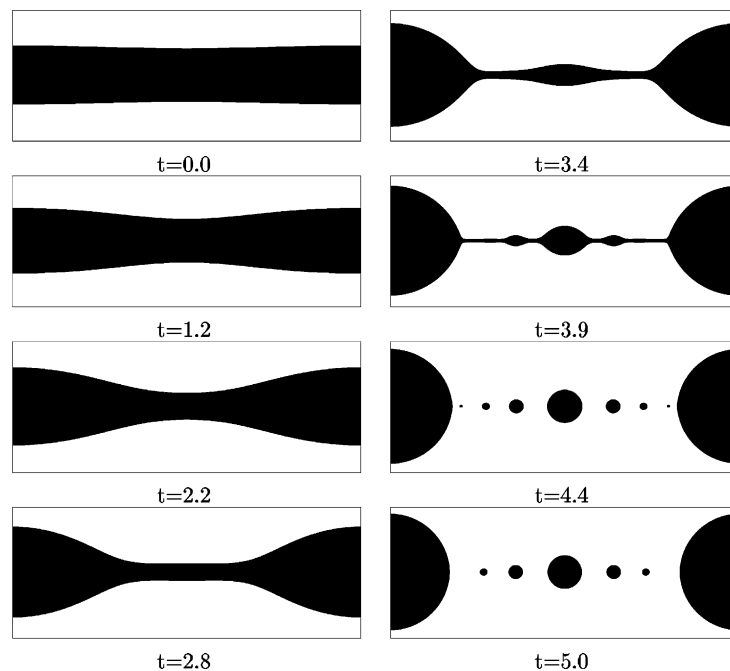


Fig. 11. Time evolution of a liquid/liquid thread undergoing the Rayleigh instability. The dimensionless times are shown below each figure.

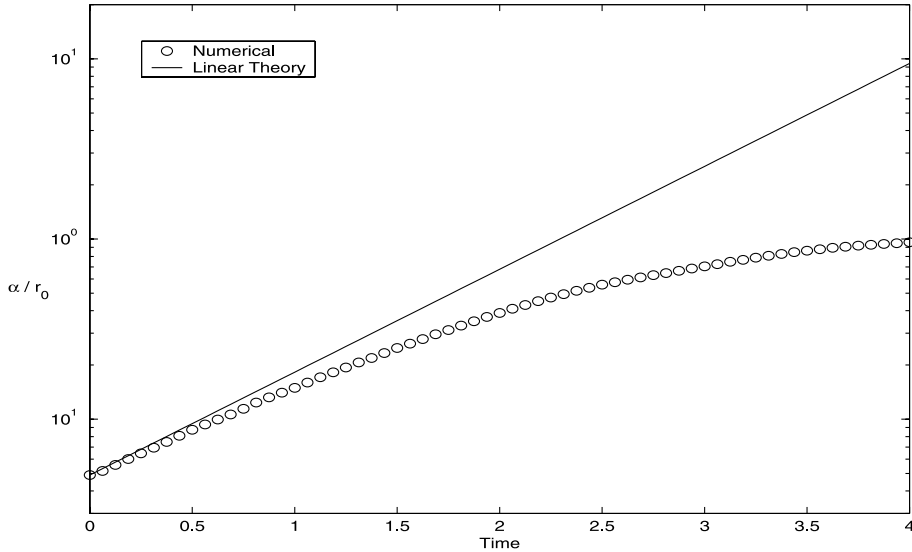


Fig. 12. Comparison of the perturbation amplitudes: ‘o’ numerical result and ‘—’ linear stability theory.

In the simulation presented in Fig. 11 only the region interior to the  $c = 0.5$  contour is shown. In the early stages ( $t = 0.0, 1.2$ , and  $2.2$ ), the interface has only one minimum at the middle of the thread. As the time increases, nonlinearity becomes important and the and two local minima develop at time  $t \approx 2.6$ . The interface grows more complex and by time  $t = 3.4$ , multiple minima develop and lead to the pinchoff of a number of satellite drops. Note that a higher resolution is needed to capture the smallest satellite drop shown at  $t = 4.4$ .

As a check on the accuracy of the simulation, we present in Fig. 12 a comparison of the growth of the perturbation from the numerical solution (circles) and from linear stability theory (solid) [52]. The numerical perturbation is determined by averaging the maximum and minimum values of the interface described by the  $c = 0.5$  contour. At early times, when the perturbation is small, there is excellent agreement between the theory and simulation. The results deviate when nonlinearity becomes important. This will be investigated in more detail in [23].

## Acknowledgements

The first (J.K.) and third (J.L.) authors acknowledge the support of the Department of Energy, Office of Basic Energy Sciences. J.L. also acknowledges the support of the National Science Foundation, Division of Mathematical Sciences. The second author (K.K.) was partially supported by NSF Grant No. DMS-9877055 and he thanks Professor B. Cockburn for helpful discussions. The authors are also grateful for the support of the Minnesota Supercomputer Institute and the Institute for Mathematics and its Applications.

## Appendix A. Smoothing operator

The derivation of the SMOOTH relaxation operator given in Eqs. (31) and (32) is as follows. Rewriting (13), we get

$$\frac{c_{ij}^{n+1}}{\Delta t} + \left( \frac{2}{\Delta x^2} + \frac{2}{\Delta y^2} \right) \mu_{ij}^{n+\frac{1}{2}} = \frac{\mu_{i+1,j}^{n+\frac{1}{2}} + \mu_{i-1,j}^{n+\frac{1}{2}}}{\Delta x^2} + \frac{\mu_{i,j+1}^{n+\frac{1}{2}} + \mu_{i,j-1}^{n+\frac{1}{2}}}{\Delta y^2} + \frac{c_{ij}^n}{\Delta t}. \quad (\text{A.1})$$

By Eq. (14),

$$-\frac{\epsilon^2}{2} \left( \frac{2}{\Delta x^2} + \frac{2}{\Delta y^2} \right) c_{ij}^{n+1} + \mu_{ij}^{n+\frac{1}{2}} = -\frac{\epsilon^2}{2} \Delta_d c_{ij}^n + \hat{\phi}(c_{ij}^n, c_{ij}^{n+1}) - \frac{\epsilon^2}{2\Delta x^2} (c_{i+1,j}^{n+1} + c_{i-1,j}^{n+1}) - \frac{\epsilon^2}{2\Delta y^2} (c_{i,j+1}^{n+1} + c_{i,j-1}^{n+1}). \quad (\text{A.2})$$

Since  $\hat{\phi}(c_{ij}^n, c_{ij}^{n+1})$  is nonlinear with respect to  $c_{ij}^{n+1}$ , we linearize  $\hat{\phi}(c_{ij}^n, c_{ij}^{n+1})$  at  $c_{ij}^m$

$$\hat{\phi}(c_{ij}^n, c_{ij}^{n+1}) = \hat{\phi}(c_{ij}^n, c_{ij}^m) + \frac{\partial \hat{\phi}(c_{ij}^n, c_{ij}^m)}{\partial c_2} (c_{ij}^{n+1} - c_{ij}^m).$$

After substitution of this into (A.2), we replace  $c^{n+1}$  and  $\mu^{n+\frac{1}{2}}$  in Eqs. (A.1) and (A.2) with  $c^{m+1}$  and  $\mu^{m+\frac{1}{2}}$ , to obtain the relaxation scheme:

$$\frac{c_{ij}^{m+1}}{\Delta t} + \left( \frac{2}{\Delta x^2} + \frac{2}{\Delta y^2} \right) \mu_{ij}^{m+\frac{1}{2}} = \frac{\mu_{i+1,j}^{m+\frac{1}{2}} + \mu_{i-1,j}^{m+\frac{1}{2}}}{\Delta x^2} + \frac{\mu_{i,j+1}^{m+\frac{1}{2}} + \mu_{i,j-1}^{m+\frac{1}{2}}}{\Delta y^2} + \frac{c_{ij}^n}{\Delta t}, \quad (\text{A.3})$$

and

$$\begin{aligned} -\left[ \frac{\epsilon^2}{2} \left( \frac{2}{\Delta x^2} + \frac{2}{\Delta y^2} \right) + \frac{\partial \hat{\phi}(c_{ij}^n, c_{ij}^m)}{\partial c_2} \right] c_{ij}^{m+1} + \mu_{ij}^{m+\frac{1}{2}} = & -\frac{\epsilon^2}{2} \Delta_d c_{ij}^n + \hat{\phi}(c_{ij}^n, c_{ij}^m) - \frac{\partial \hat{\phi}(c_{ij}^n, c_{ij}^m)}{\partial c_2} c_{ij}^m \\ & - \frac{\epsilon^2}{2\Delta x^2} (c_{i+1,j}^m + c_{i-1,j}^m) - \frac{\epsilon^2}{2\Delta y^2} (c_{i,j+1}^m + c_{i,j-1}^m), \quad (\text{A.4}) \end{aligned}$$

as claimed in Section 4.

## Appendix B. Crank–Nicholson scheme

Here, we present another scheme in which

$$\hat{\phi}(c^n, c^{n+1}) = \frac{1}{2}(\phi(c^n) + \phi(c^{n+1})).$$

This results in the traditional Crank–Nicolson scheme:

$$\begin{aligned} \frac{c_{ij}^{n+1} - c_{ij}^n}{\Delta t} &= \Delta_d \mu_{ij}^{n+\frac{1}{2}}, \\ \mu_{ij}^{n+\frac{1}{2}} &= \frac{1}{2}(\phi(c_{ij}^{n+1}) + \phi(c_{ij}^n)) - \frac{\epsilon^2}{2} \Delta_d (c_{ij}^{n+1} + c_{ij}^n). \end{aligned}$$

This algorithm extends straightforwardly to the ternary case and the nonlinear multigrid method given in Section 4 also can be modified to solve the new nonlinear system at the implicit time-level. Moreover, at the linear level (i.e.,  $\phi$  is a linear function), this scheme is the same as that considered in the body of the paper. However, at the nonlinear level, we are unable to prove that the system given above has a discrete energy function unless a second-order time step constraint is imposed. This constraint is much stronger than that needed for stability and seems to be a shortcoming of the analysis as simulation results using the traditional Crank–Nicolson scheme always yield non-increasing discrete energies.



## References

- [1] D. Anderson, G.B. McFadden, A.A. Wheeler, Diffuse interface methods in fluid mechanics, *Ann. Rev. Fluid Mech.* 30 (1998) 139.
- [2] J. Lowengrub, L. Truskinovsky, Quasi-incompressible Cahn–Hilliard fluids and topological transitions, *R. Soc. Lond. Proc. Ser. A Math. Phys. Eng. Sci.* 454 (1978) (1998) 2617.
- [3] J.-S. Kim, K. Kang, J. Lowengrub, Conservative multigrid methods for ternary Cahn–Hilliard fluids, *Comm. Math. Sci.* (in review).
- [4] J.J. Eggleston, G.B. McFadden, P.W. Voorhees, A phase field model for highly anisotropic interfacial energy, *Phys. D* 150 (2001) 91.
- [5] D. Jacqmin, Calculation of two-phase Navier–Stokes flows using phase-field modeling, *J. Comput. Phys.* 155 (1999) 96.
- [6] B. Nadiga, S. Zaleski, Investigations of a two-phase fluid model, *Eur. J. Mech. B/Fluids* 15 (1996) 885.
- [7] J. Hageman, A study of pinchoff and reconnection of an unstably stratified fluid layer, M.S. Thesis, Department of Aerospace and Mechanics, University of Minnesota, 1999.
- [8] J. Lowengrub, J. Goodman, H. Lee, E. Longmire, M. Shelley, L. Truskinovsky, Topological Transitions in Liquid/Liquid Interfaces, Chapman & Hall/CRC Res. Notes Math, 1999, p. 221.
- [9] E.K. Longmire, J. Lowengrub, D.L. Gefroh, A comparison of experiments and simulations on pinch-off in round jets, in: Proceedings of the 1999 ASME/JSME Meeting, San Francisco.
- [10] D. Jasnow, J. Vinals, Coarse-grained description of thermocapillary flows, *Phys. Fluids* 8 (1996) 660.
- [11] M. Vershueren, F.N. vande Vosse, H.E.H. Meijer, Diffuse-interface modeling of thermocapillary flow instabilities in a Hele–Shaw cell, *J. Fluid Mech.* 434 (2001) 153.
- [12] R. Chella, J. Vinals, Mixing of a two-phase fluid by cavity flow, *Phys. Rev. E* 53 (1996) 3832.
- [13] D. Jacqmin, Contact line dynamics of a diffuse interface, *J. Fluid Mech.* 402 (2000) 57.
- [14] P. Seppacher, Moving contact lines in the Cahn–Hilliard theory, *Int. J. Eng. Sci.* 34 (1996) 977.
- [15] D. Anderson, G.B. McFadden, A diffuse-interface description of internal waves in a near critical fluid, *Phys. Fluids* 9 (1997) 1870.
- [16] L. de Sobrino, Note on capillary waves in the gradient theory of interfaces, *Can. J. Phys.* 63 (1985) 1132.
- [17] L. de Sobrino, J. Peternelj, On capillary waves in the gradient theory of interfaces, *Can. J. Phys.* 63 (1985) 131.
- [18] M. Vershueren, A diffuse interface model for structure development in flow, Ph.D. Thesis, Technische Universiteit Eindhoven, the Netherlands, 1999.
- [19] H. Struchtrup, J.W. Dold, Surface tension in a reactive binary mixture of incompressible fluids, IMA preprint 1708, 2000.
- [20] F. Dell’Isola, H. Gouin, G. Rotoli, Radius and surface tension of microscopic bubbles by second gradient theory, *Eur. J. Mech. B/Fluids* 15 (1996) 545.
- [21] F. Dell’Isola, H. Gouin, P. Seppacher, Nucleation of spherical shell-like interfaces by second gradient theory: numerical simulations, *C.R. Acad. Sci. Paris* 320 (1995) 211.
- [22] M.E. Gurtin, D. Polignone, J. Vinals, Two-phase binary fluids and immiscible fluids described by an order parameter, *Math. Models Methods Appl. Sci.* 6 (1996) 815.
- [23] J.-S. Kim, J. Lowengrub, On the pinchoff of liquid/liquid jets with surface tension, in preparation.
- [24] P.C. Hohenberg, B.I. Halperin, Theory of dynamic critical phenomena, *Rev. Mod. Phys.* 49 (1977) 435.
- [25] D. Brown, R. Cortez, M. Minion, Accurate projection methods for the incompressible Navier–Stokes equations, *J. Comput. Phys.* 168 (2001) 168.
- [26] J.W. Cahn, On spinodal decomposition, *Acta Metall.* 9 (1961) 795.
- [27] A.S. Almgren, J.B. Bell, W.G. Szymczak, A numerical method for the incompressible Navier–Stokes equations based on an approximate projection, *SIAM J. Sci. Comput.* 17 (2) (1996) 358.
- [28] A.S. Almgren, J.B. Bell, P. Colella, L.H. Howell, M.L. Welcome, A conservative adaptive projection method for the variable density incompressible Navier–Stokes equations, *J. Comput. Phys.* 142 (1) (1998) 1.
- [29] J.W. Barrett, J.F. Blowey, Finite element approximation of a model for phase separation of a multi-component alloy with non-smooth free energy, *Numer. Math.* 77 (1) (1997) 1.
- [30] J.W. Barrett, J.F. Blowey, Finite element approximation of the Cahn–Hilliard equation with concentration dependent mobility, *Math. Comp.* 68 (226) (1999) 487.
- [31] J.W. Barrett, J.F. Blowey, An optimal error bound for a finite element approximation of a model for phase separation of a multi-component alloy with non-smooth free energy, *M2AN Math. Model. Numer. Anal.* 33 (5) (1999) 971.
- [32] J.W. Barrett, J.F. Blowey, H. Garcke, Finite element approximation of the Cahn–Hilliard equation with degenerate mobility, *SIAM J. Numer. Anal.* 37 (1) (1999) 286.
- [33] H. Garcke, M. Rumpf, U. Weikard, The Cahn–Hilliard equation with elasticity: Finite element approximation and quantitative studies, *Int. Free Bound.* (in press).
- [34] J.W. Barrett, J.F. Blowey, Finite element approximation of an Allen–Cahn/Cahn–Hilliard system, *IMA J. Numer. Anal.* 22 (1) (2002) 11.
- [35] J.W. Cahn, J.E. Hilliard, Free energy of a nonuniform system. I. Interfacial free energy, *J. Chem. Phys.* 28 (1958) 258.

- [36] M. Copetti, Numerical experiments of phase separation in ternary mixtures, *Math. Comput. Simulation* 52 (1) (2000) 41.
- [37] M. Copetti, C.M. Elliott, Kinetics of phase decomposition processes: numerical solutions to the Cahn–Hilliard equation, *Mater. Sci. Technol.* 6 (1990) 273.
- [38] C. Elliott, The Cahn–Hilliard model for the kinetics of phase separation, in: J. Rodrigues (Ed.), *Mathematical Models for Phase Change Problems*, International Series of Numerical Mathematics, 88, Birkhäuser, Basel, 1989.
- [39] C. Elliott, D. French, Numerical studies of the Cahn–Hilliard equation for phase separation, *IMA J. Appl. Math.* 38 (1987) 97.
- [40] C.M. Elliott, Stig. Larsson, Error estimates with smooth and nonsmooth data for a finite element method for the Cahn–Hilliard equation, *Math. Comp.* 58 (198) 603; S33 (1992).
- [41] C.M. Elliott, D.A. French, A nonconforming finite-element method for the two-dimensional Cahn–Hilliard equation, *SIAM J. Numer. Anal.* 26 (4) (1989) 884.
- [42] C. Elliott, D. French, F. Milner, A second order splitting method for the Cahn–Hilliard equation, *Numer. Math.* 54 (1989) 575.
- [43] D.J. Eyre, Systems for Cahn–Hilliard equations, *SIAM J. Appl. Math.* 53 (1993) 1686.
- [44] D.A. French, J.W. Schaeffer, Continuous finite element methods which preserve energy properties for nonlinear problems, *Appl. Math. Comput.* 39 (3) (1990) 271.
- [45] D. Furihata, Finite difference schemes for  $\frac{\partial u}{\partial t} = \left(\frac{\partial}{\partial x}\right)^{\alpha} \frac{\partial G}{\partial u}$  that inherit energy conservation or dissipation property, *J. Comput. Phys.* 156 (1999) 181.
- [46] D. Furihata, Daisuke A stable and conservative finite difference scheme for the Cahn–Hilliard equation, *Numer. Math.* 87 (4) (2001) 675.
- [47] H.Y. Lee, J. Lowengrub, J. Goodman, Modeling pinchoff and reconnection in a Hele–Shaw cell. I. The models and their calibration, *Phys. Fluids* 14 (2) (2002) 492.
- [48] H.Y. Lee, J. Lowengrub, J. Goodman, Modeling pinchoff and reconnection in a Hele–Shaw cell. II. Analysis and simulation in the nonlinear regime, *Phys. Fluids* 14 (2) (2002) 514.
- [49] F. Daniel Martin, Phillip Colella, A cell-centered adaptive projection method for the incompressible Euler equations, *J. Comput. Phys.* 163 (2000) 271.
- [50] Z.Z. Sun, A second-order accurate linearized difference scheme for the two-dimensional Cahn–Hilliard equation, *Math. Comp.* 64 (212) (1995) 1463.
- [51] R. Temam, *Infinite Dimensional Dynamical Systems in Mechanics and Physics*, Springer, New York, 1988.
- [52] Tomotika, On the instability of a cylindrical thread of a viscous liquid surrounded by another viscous fluid, *Proc. Roy. Soc. A* 150 (1935) 322.
- [53] U. Trottenberg, C. Oosterlee, A. Schüller, *MULTIGRID*, Academic Press, New York, 2001.
- [54] S. Zheng, Asymptotic behavior of the solution to the Cahn–Hilliard equation, *Appl. Anal.* 23 (1986) 165.
- [55] S. Osher, R. Fedkiw, Level set methods: An overview and some recent results, *J. Comput. Phys.* 169 (2001) 463.
- [56] J.A. Sethian, P. Smereka, Level set methods for fluid interfaces, *Ann. Rev. Fluid Mech.* 35 (2003) 341.
- [57] R. Scardovelli, S. Zaleski, Direct numerical simulation of free surface and interfacial flow, *Ann. Rev. Fluid Mech.* 31 (1999) 576.
- [58] M. Sussman, A. Almgren, J. Bell, P. Colella, L. Howell, M. Welcome, An adaptive level set approach for incompressible two-phase flows, *J. Comput. Phys.* 148 (1999) 81.
- [59] V. Cristini, J. Lowengrub, X. Zheng and T. Anderson, An algorithm for adaptive remeshing of 2D and 3D domains: Application to the level-set method, in preparation.